Petroleum Science 22 (2025) 4875–4894

Contents lists available at ScienceDirect

Petroleum Science

journal homepage: www.keaipublishing.com/en/journals/petroleum-science

Original Paper

The control of astronomical cycles on lacustrine mixed sedimentation and hydrocarbon occurrence: A case study of the Paleogene Shahejie Formation in the Dongying Sag, Bohai Bay Basin

Xian-Xu Fang [a,b], Cun-Fei Ma [a,b,*], Feng Qin [c], Tian-Xia An [c], Rui-Juan Liu [c], Hao-Wen Song [a,b], Cun-Jian Zhang [a,b], Tao Wang [a,b], Bo Gao [b,d], Peng Hao [e]

[a] State Key Laboratory of Deep Oil and Gas, China University of Petroleum (East China), Qingdao, 266580, Shandong, China
[b] School of Geosciences, China University of Petroleum (East China), Qingdao, 266580, Shandong, China
[c] Petroleum Exploration and Production Research Institute, Sinopec Shengli Oilfield, Dongying, 257000, Shandong, China
[d] Binnan Oil Production Plant, Sinopec Shengli Oilfield, Binzhou, 256600, Shandong, China
[e] CNOOC Experimental Center, CNOOC EnerTech-Driling & Production Co., Tianjin, 300452, China

A R T I C L E I N F O

Article history:
Received 3 December 2024
Received in revised form
2 June 2025
Accepted 3 September 2025
Available online 9 September 2025

Edited by Xi Zhang and Jie Hao

Keywords:
Mixed gravity flow-shale depositional model
Conventional-unconventional hydrocarbon coexistence
Lithofacies combinations
Astronomical cycles
Paleogene Shahejie Formation
Steep-slope lacustrine rift basins

A B S T R A C T

Gravity flows in steep-slope zones of lacustrine rift basins interact with deep-water shales to form heterogeneous mixed sedimentation zones, yet their sedimentary evolution and hydrocarbon occurrence characteristics remain poorly understood. In this study, core and thin section observations, X-ray diffraction, scanning electron microscopy, mercury intrusion porosimetry, low-pressure nitrogen physisorption, total organic carbon testing, step-by-step Rock-Eval pyrolysis, and time series analysis, were conducted to decode sedimentology and hydrocarbon occurrence characteristics based on lithofacies combinations controlled by astronomical cycles. Results reveal five microfacies (calcareous/felsic semi-deep lake, outer fan, channel front, braided channel) and six lithofacies combinations (LC1–LC6) shaped by debris flows, turbidity currents, and felsic mixed floating currents. The 406-kyr long eccentricity cycle governs sediment supply and reservoir heterogeneity. During high eccentricity phases, increased monsoon-driven terrigenous input enhances sandstone deposition, developing braided channel (LC5) and channel front (LC6) microfacies. These intervals exhibit elevated terrigenous quartz/feldspar content and reduced organic carbon in fine-grained sedimentary rocks, with hydrocarbons occurring as quasi-continuous to discontinuous accumulations. Conversely, during low eccentricity phases, felsic mineral layers or isolated sandstone interlayers dominate, forming outer fan (LC3), channel front (LC4), and semi-deep lake (LC1–LC2) microfacies. These intervals show lower terrigenous content and higher TOC in fine-grained sedimentary rocks, with hydrocarbons occurring as continuous to quasi-continuous accumulations. A novel sedimentary evolution and hydrocarbon occurrence model demonstrates the ordered coexistence of conventional and unconventional reservoirs, driven by astronomically forced climate fluctuations. This framework advances theoretical understanding and optimizes exploration strategies for steep-slope lacustrine basins with mixed sedimentation.

1. Introduction

In recent years, the study of mixed sedimentation has become a key focus in the field of sedimentology. The concept of Mixed Sedimentation (Mount, 1984) is a universal and complex geological process. It refers to a sediment comprised of a mixture of different components (terrigenous detritus and carbonate rock) or varying grain sizes (Garcia-Hidalgo et al., 2007; Palermo et al., 2008; Yerejiepu et al., 2024). It is believed that the black shale is deposited in a deep, quiet and anoxic bottom-water environment, and is almost undisturbed (Hou et al., 2023; Lineback, 1968; Smith et al., 2019). However, bottom current, turbidity current and debris flow are common hydrodynamics in deep water and may affect shale deposition (Alexandre et al., 2012; Chao et al., 2016; Hou

* Corresponding author.
E-mail address: mcf-625@163.com (C.-F. Ma).
Peer review under the responsibility of China University of Petroleum (Beijing).

https://doi.org/10.1016/j.petsci.2025.09.005

et al., 2023; Liu et al., 2019; Loucks and Ruppel, 2007). For example, due to emergencies such as earthquakes, floods or storms, gravity flow can transport debris from the continental shelf or upper slope to deep-water areas and mix with shale sediments (Hou et al., 2023; Loucks and Ruppel, 2007; Yerejiepu et al., 2024). Compared with the marine environment, the lacustrine sedimentary environment is particularly vulnerable to external factors such as tectonic movements, climate changes, earthquakes, floods, and storms (Palermo et al., 2008; Yerejiepu et al., 2024), and mixed sedimentation caused by these events often occurs more frequently (Dodd et al., 2019; Feng et al., 2021; Niu et al., 2023; Wang et al., 2020a; Yerejiepu et al., 2024).

Recent advancements in lithofacies analysis have significantly enhanced the understanding of depositional processes and reservoir heterogeneity in shale-dominated successions (Liu et al., 2019; Plantz et al., 2024). Notably, studies increasingly emphasize the critical role of sedimentary structures—such as interlayers, laminations, and deformation features—in refining lithofacies identification and predicting hydrocarbon sweet spots (Chen et al., 2017; Ougier-Simonin et al., 2016; Shu et al., 2021). These structures, often linked to dynamic processes like turbidity currents, debris flows, or seasonal sedimentation, directly influence organic matter preservation, porosity distribution, and fracture networks (Liang et al., 2017; Zou, 2017). In lacustrine rift basins, where steep slopes and mixed sedimentation dominate, lithofacies combinations (e.g., alternating organic-rich shales, siltstones, and carbonate-rich layers) encode key information about depositional energy, redox conditions, and sediment supply cyclicity (Liang et al., 2024). Deciphering these relationships is pivotal for unraveling shale oil enrichment mechanisms and optimizing exploration strategies. While prior works have focused on either lithofacies or sedimentary structures in stable settings, few address their synergistic roles in mixed sedimentation systems with abrupt facies transitions. In petroliferous basins, conventional oil and gas reservoirs and unconventional oil and gas reservoirs, or continuous, quasi-continuous and discontinuous reservoirs often coexist, indicating that they have a close relationship and share a unique distribution law (Chen et al., 2021; Law and Curtis, 2002; Masters, 1979; Pang et al., 2021; Selley and Sonnenberg, 2015; Zhao et al., 2017). Mixed sedimentation usually occurs in the transition zone between different sedimentary facies, representing a form of facies mixing, as well as the mixing form between conventional and unconventional oil and gas reservoirs. The development of mixed sedimentation significantly increases the heterogeneity of the reservoir, which may have a negative impact on oil and gas exploration (Yerejiepu et al., 2024). In order to promote the exploration of conventional and unconventional reservoirs, it is necessary and important to carry out the research on the hydrocarbon occurrence characteristics of mixed sedimentations (Law, 2002; Pang et al., 2021; Xi et al., 2015; Zagorski, 1988; Zhang et al., 2018).

Due to the stability and continuity of lacustrine fine-grained deposition, obvious signals of the Milankovitch cycles have been identified in lacustrine deposits worldwide (Abels et al., 2009, 2013; Colcord et al., 2018; Huang et al., 2010; Machlus et al., 2008; Pälike et al., 2001; Shi et al., 2020; Wu et al., 2014), and astronomical cycles have been shown to control the depositional processes of fine-grained sedimentary rocks in lake basins (Shi et al., 2020; Smith et al., 2014). The distribution of event sedimentation is mostly controlled by water depths and climate changes, which are related to astronomical cycles (Chen et al., 2021; Xu et al., 2023). Although some studies were conducted on the relationship between astronomical cycles and event sedimentation (Wang et al., 2015; Xu et al., 2023), there are limited studies on the relationship between mixed sedimentation and astronomical cycles in the case of integrating fine-grained sedimentary rocks with event sedimentation. Therefore, it restricts the further exploration of the control factors and distribution rules of mixed sedimentation, thereby hindering the effective integration of conventional and unconventional oil and gas exploration.

The Meso-Cenozoic lacustrine rift basins, including the Dongying Sag in the Bohai Bay Basin, cover a total area of over 2×10^6 km^2 in eastern China (Cao et al., 2018; Guo et al., 2012; Wang et al., 2014; Xian et al., 2007). The basin boundaries of these lacustrine rift basins are mainly controlled by faults and have steep slope zones. The steep slope zone has a steep topographic gradient along the high-angle fault plane (up to about 30°) and enough subaqueous accommodation space, which is generated by the episodic movement of boundary faults and used for deep-water deposition (Cao et al., 2018). These tectonic conditions determine the extensive development of various genetic types of fans, such as nearshore subaqueous fans, sublacustrine fans, and turbidite fans. In the steep slope zone in the northern Dongying Sag, the nearshore subaqueous fans have an excellent source-reservoir-cap combination, forming abundant conventional reservoirs (Guo et al., 2012; Kouassi et al., 2022). And the shale near the deep lake is thick, forming abundant unconventional reservoirs. The Paleogene Shahejie Formation, located in the mixed sedimentation zone of the nearshore subaqueous fans and deep-lacustrine fine-grained sediments, contains thick black shale and well-developed gravity flow deposits, which provides a good opportunity to study the impact of gravity flow on shale development and hydrocarbon occurrence characteristics in lacustrine settings under the control of astronomical cycle. The area is less affected by geological tectonics, and the fine-grained sedimentary rocks are sensitive to climate change, making it suitable for identifying astronomical cycle signals (Xu et al., 2023). Based on the identification of Milankovitch cycles, previous studies have made some progress in high-frequency sequence delineation, relative lake level variation, optimal sedimentation rate, paleoclimatic and paleoenvironmental variation restoration in the Dongying Sag (Jin et al., 2022; Shi et al., 2019, 2020; Sun et al., 2017; Xu et al., 2023).

The oil and gas production data show that there are significant differences in the hydrocarbon occurrence content of different types of lithofacies combinations. The sedimentary process and distribution of each lithofacies combination are not clear, which restricts the deployment of oil and gas exploration in the northern steep slope zone of Dongying Sag. Therefore, based on the study of the main oil production members (the upper fourth member and the lower third member of the Eocene Shahejie Formation) in the mixed sedimentation zone in the northern steep slope zone of Dongying Sag, the objectives of this research are: (i) to identify the types of lithofacies combinations and sedimentary microfacies and propose a new depositional model for the mixed sedimentation zone in lacustrine rift basins with steep slopes; (ii) to identify hydrocarbon occurrence content of different lithofacies combinations and propose a sedimentary evolution and hydrocarbon occurrence model for transition zone controlled by astronomical cycles.

2. Geologic background

The Bohai Bay Basin, established on the Archean basement, is a Mesozoic-Cenozoic rift basin including many continental subbasins in the North China Craton (Kouassi et al., 2022; Wang et al., 2016a). The Dongying Sag lies in the south-eastern part of the Jiyang Depression of the Bohai Bay Basin (Cao et al., 2018). It is a Cenozoic half-graben rift and down-warped lacustrine basin developed over a Palaeozoic basement (Cao et al., 2018). In planar view in Fig. 1(a), the Dongying Sag is further subdivided into

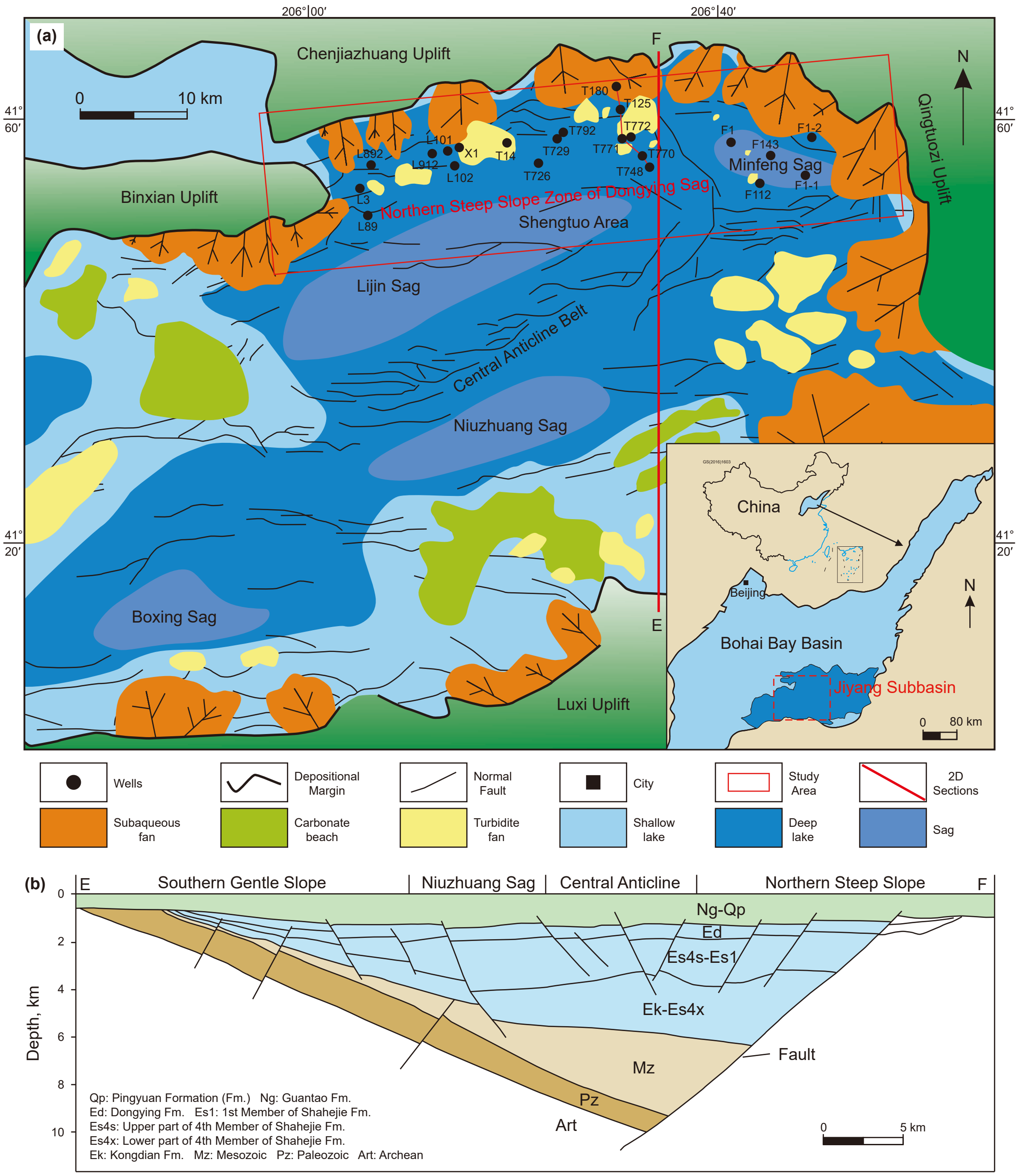

Fig. 1. **(a)** Structural map and facies distribution during deposition of the lower Es3 Member of the Dongying Sag of the Jiyang Depression showing locations of the study area and cross-section E–F. **(b)** Structural cross-section across the Dongying Depression based on seismic profiles showing the various tectonic-structural zones and key stratigraphic intervals (modified from Guo et al., 2012; Cao et al., 2018; Liu et al., 2018; Wang et al., 2020b).

several secondary structural units including the northern steep slope, the central anticline, the Niuzhuang Sag, and the southern gentle slope (Cao et al., 2018; Jiang et al., 2014; Kouassi et al., 2022; Ping et al., 2017). In cross-section in Fig. 1(b), the Dongying Sag is a half graben with a fault-controlled northern steep slope and a southern gentle slope (Cao et al., 2018). Located north of the Northern Sag zone, west of the Qingtuozi uplift, south of the Chenjiazhuan uplift (Lijin Sag, Shengtuo Area and Minfeng Sag), and east of the Binxian uplift, the northern steep slope zone of Dongying Sag covers a surface of 2000 km^2 (Guo et al., 2012; Ma et al., 2017; Ping et al., 2017; Yang et al., 2018).

The Palaeogene of the northern steep slope zone of the Dongying Sag can be divided into Kongdian (Ek), Shahejie (Es) and Dongying (Ed) formations from bottom to top (Fig. 2). The Shahejie Formation can be further divided from bottom to top into four members including the Fourth Member (Es4), the Third Member (Es3), the Second Member (Es2) and the First Member (Es1), respectively (Cao et al., 2018). Member Es4 consists of an upper part (Es4s) and a lower part (Es4x) and Member Es3 consists of an upper part (Es3s), a middle part (Es3z), and a lower part (Es3x). The upper Es4 (Es4s) and the lower Es3 (Es3x) contain the main source rocks and sandstone reservoir rocks. The upper Es4 (Es4s) consists of intercalations of brown-grey, grey to black shale, calcareous shale, calcareous mudstones, mudstone, dolomite, as well as marlstone. The lower Es3 (Es3x) interval is dominated by lacustrine oil shales, dark-grey mudstones and calcareous mudstones and is an important source rock within the Dongying Sag (Guo et al., 2012). Astronomically-forced climate cycles, widely recognized in sedimentary records of the Bohai Bay Basin, provide critical tools for refining geological timescales. In a landmark study, Shi et al. (2019) constructed a high-resolution cyclostratigraphic framework for the Es3x to Es4s interval in the Dongying Sag by integrating new paleomagnetic data from Well Fanye-1, which established an absolute age range of 43.27–39.23 Ma for the studied section. Their work precisely constrained the Es3–Es4 boundary age to 41.38 Ma (Fig. 2) – a value adopted in this study as the chronostratigraphic anchor for correlating equivalent strata (Fig. 2).

During the accumulation of the Es4 and Es3, controlled by the ancient tectonic background of a rift stage, terrigenous sediments were transported to deep waters by debris flows, mountain-derived floods and normal mountain-derived river discharges during non-flood periods (Cao et al., 2018; Wang et al., 2016b). In the northern steep slope zone, large-scale sediments of near-shore subaqueous fans and fan deltas formed close to deep-water source rocks (Kouassi et al., 2022; Wang et al., 2014). The study area is located in the mixed sedimentation zone between gravity flow sediments and deep-lacustrine fine-grained sediments, which is also the transition zone between conventional and unconventional reservoirs.

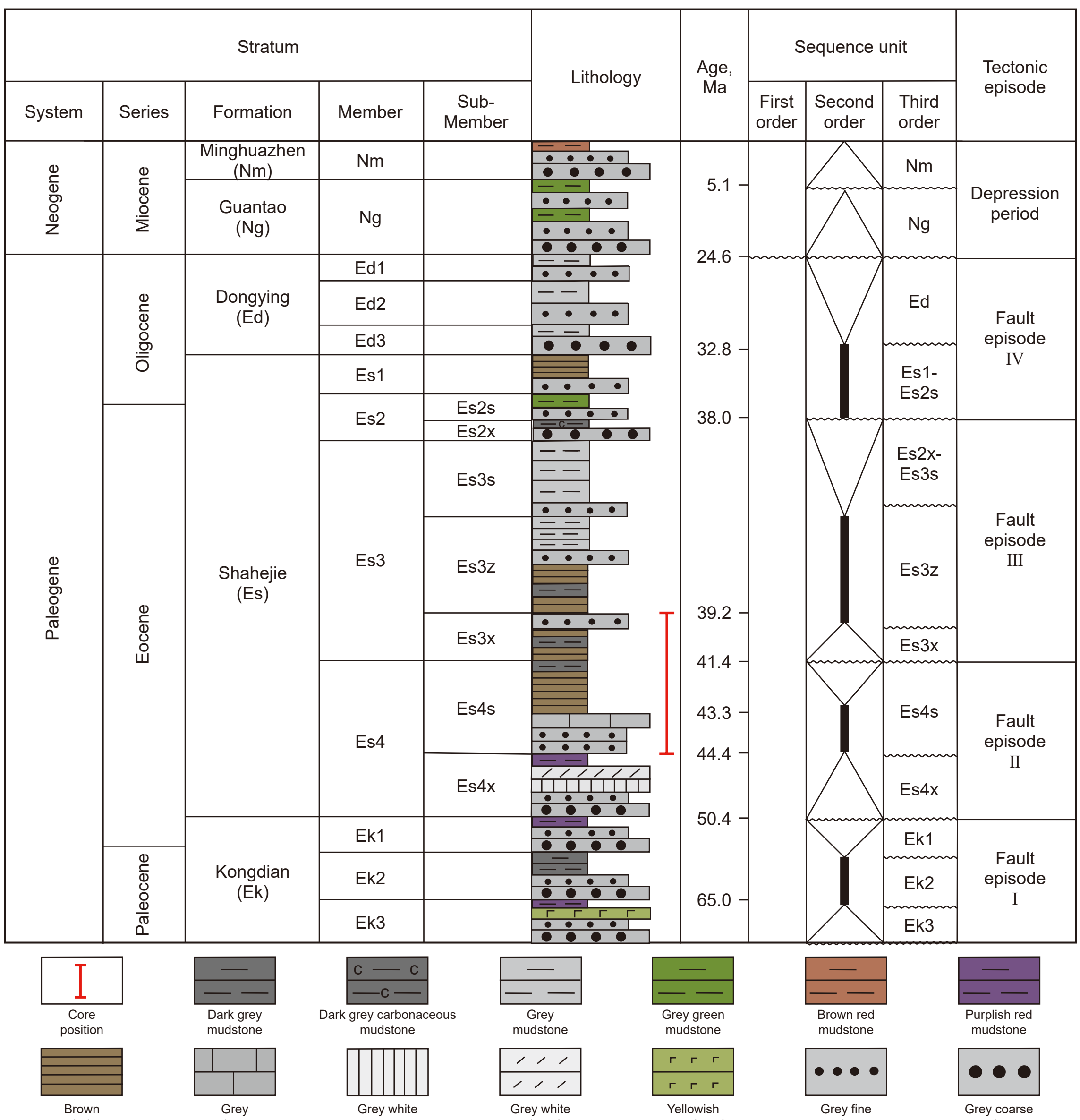

Fig. 2. Cenozoic stratigraphy chart and timescales of the Dongying Sag (modified from Fang et al., 2024; ages of the Shahejie Formation in the Jiyang Depression according to Shi et al., 2019; Jin et al., 2022).

3. Samples and methods

3.1. Samples

Eighteen Wells (F112, F143, F1, F1-1, F1-2, L89, L912, L3, L101, L102, L892, X1, T14, T726, T729, T771, T772, T792) with core through the Lower Member 3 and the Upper Member 4 of the Shahejie Formation were selected from the northern steep slope of Dongying Sag, Bohai Bay Basin in Fig. 1(a). The total length of continuous coring for these wells is 1408.39 m, and core observations on all of them for sedimentological analysis have been conducted. Based on properties such as sedimentary facies, sedimentary texture, and oil content, 104 samples were selected from drilling cores of 18 wells for thin-section petrographical analysis. Forty representative samples were prepared for X-ray diffraction (XRD), FE-SEM, mercury intrusion porosimetry (MIP), low-pressure nitrogen physisorption (LPNP), total organic carbon testing (TOC), step-by-step (SBS) Rock-Eval pyrolysis. The well data, such as gamma ray logging data, were collected from the Petroleum Exploration and Production Research Institute of China Sinopec Shengli Oilfield Company. Other than specifically stated, all analyses were performed in the State Key Laboratory of Deep Oil and Gas, China University of Petroleum (East China).

3.2. XRD mineralogy, thin section petrography and FE-SEM observations

Powdered rock samples with a size of less than #200 mesh were analyzed by XRD for bulk mineral composition by the PANalytical X'Pert PRO MPD (PANalytical B.V., NL) X-ray diffractometer. Petrographical analysis focused on the identification of mineral type, particle structure, fluorescence recognition of hydrocarbon occurrence and two-dimensional features of micro-sedimentary structure within the mud-grade sediments, using a Zeiss microscope and a scanning electron microscope (Zeiss Crossbeam 550 FIB-SEM; Carl Zeiss AG, Oberkochen, Germany).

3.3. Mercury intrusion porosimetry (MIP)

The Micromeritics AutoPore IV 9520 MIP instrument (Micromeritics, USA) can obtain many parameters such as bulk density, porosity, pore throat size distribution, permeability and tortuosity in various porous media (Hu et al., 2017; Katz and Thompson, 1987; Wang et al., 2016c; Washburn, 1921; Zhang et al., 2024a). The samples were cubes of 1 cm in length and were dried in an oven at 60 °C for more than 48 h to remove moisture and volatiles from the connected pore space (Zhang et al., 2024a).

3.4. Low-pressure nitrogen physisorption (LPNP)

LPNP was performed using a Micromeritics ASAP 2460 Surface Area and Porosimetry Analyzer to obtain pore volume, specific surface area (SSA) and pore size distribution of rock samples. Samples of 20–35 mesh were dried in an oven at 110 °C for 24 h, and then degassed with a sample degassing system at the same temperature for 24 h to remove moisture and volatiles in the connected pore space (Zhang et al., 2024a). The physical adsorption isotherm of nitrogen was obtained at −195.85 °C, and a low-voltage sensor can determine the pore size distribution in the diameter range of 2–300 nm (Zhang et al., 2024a). The SSA of shale samples was calculated by the Brunauer-Emmett-Teller (BET) method (Brunauer et al., 1938), and the pore volume and pore size distribution were calculated by Barrett-Joyner-Halenda (BJH) method based on Kelvin equation (Barrett et al., 1951; Gregg and Sing, 1982). After the first LPNP, the sample underwent solvent extraction with a mixture of dichloromethane and methanol (the volumetric ratio is 93:7) at 48 °C for at least ten days (Yang et al., 2021; Zhang et al., 2024a), and then the second LPNP was performed to compare and characterize the pore types and sizes associated with hydrocarbon occurrence.

3.5. TOC and step-by-step (SBS) Rock-Eval pyrolysis analysis

According to the procedure described by Jarvie (1991), Leco TOC analysis was performed on powdered samples using a LECO CS744 Sulfur and Carbon Analyzer. And the SBS Rock-Eval experiment was conducted on powdered samples using a Rock-Eval 6 instrument. According to the procedure described by Li et al. (2020), SBS pyrolysis was carried out to obtain the following products at each stage (Table 1). The sample was heated from 90 °C to the first target temperature of 200 °C at a programmed heating rate of 25 °C per minute and maintained for 3 min to obtain the $S_{1\text{-}1}$ peaks, then heated from 200 °C to the second target temperature of 300 °C and maintained for 3 min to obtain the $S_{1\text{-}2a}$ peaks, and then increased from 300 °C to the third target temperature of 350 °C and maintained for 3 min to produce the $S_{1\text{-}2b}$ peaks. After the third target temperature, the powdered sample was heated from 350 to 450 °C for 3 min to produce the $S_{2\text{-}1}$ peaks, and then heated from 450 to 650 °C to obtain the $S_{2\text{-}2}$ peaks (Li et al., 2020). The sum of $S_{1\text{-}1}$ and $S_{1\text{-}2}$ represents the free hydrocarbons (FHCs), corresponding to the maximum mobile hydrocarbon content; $S_{2\text{-}1}$ is the adsorbed hydrocarbon (AHCs), and $S_{2\text{-}2}$ is the cracking hydrocarbons in kerogen. Although some unstable kerogen components are cracked at or below 450 °C, some heavy components will be cracked or evaporated at temperatures higher than 450 °C. Therefore, the SBS pyrolysis method used in this study is considered to be a reliable method to characterize the total oil content (Jiang et al., 2016; Li et al., 2020).

3.6. Time series analysis

The analysis methods of astronomical cycle stratigraphy include directly identification of lithology and time series analysis. Time series analysis mainly involves data selection and preprocessing, spectral analysis, time-frequency analysis, and correlation research of geological sequences, which is a common digital signal processing technology of astronomical cycle research via well-logging data to extract ground response information about earth orbital parameters (Ma et al., 2023a; Xu et al., 2023). Westerhold et al. (2012) conducted a comparative analysis of the La2004, La2010, and La2011 astronomical solutions, identifying discrepancies in orbital parameters prior to ~43 Ma. Their evaluation highlighted the La2010d solution as the most robust orbital model for the interval since 54 Ma. Accordingly, we selected the eccentricity (E), obliquity (T), and precession (P) parameters from the La2010d model to calculate the ETP curve using the Acycle software (Shi et al., 2019).

The gamma ray logging data of well T771 was selected because of its continuous coring of Es4s. And the linear interpolation was applied on the GR data to ensure that the sampling intervals were

Table 1
The products of SBS Rock Eval experiment.

Temperature, °C	Products	Type of hydrocarbon
90–200	$S_{1\text{-}1}$	
200–300	$S_{1\text{-}2a}$	Free hydrocarbons (FHCs)
300–350	$S_{1\text{-}2b}$	
350–450	$S_{2\text{-}1}$	Adsorbed hydrocarbons (AHCs)
450–650	$S_{2\text{-}2}$	Cracking hydrocarbons

equal. The raw GR data were detrended by subtracting the LOESS method (local regression using a 2nd degree polynomial model and weighted linear least squares) to remove the low-frequency long-term trends before spectral analysis (Li et al., 2019b; Ma et al., 2023a; Sun et al., 2023).

The Multi-Taper Method (MTM) spectral estimator was performed to obtain the spectral peaks at the mean, 90%, 95%, and 99% confidence levels with robust red noise models (Li et al., 2019b; Ma et al., 2023a; Sun et al., 2023; Thomson, 1982). The La2010 theoretical astronomical model was used to identify which of these spectral peaks detected above 99% confidence levels corresponds to the orbital eccentricity, obliquity and precession (Laskar et al., 2011; Ma et al., 2023a; Sun et al., 2023). The 406-kyr long eccentricity cycle is the most stable astronomical orbital period to the noisy terrestrial stratigraphy (Ma et al., 2023a; Sun et al., 2023). Therefore, gaussian bandpass filtering was used to isolate the MTM-identified long eccentricity cycles. And the data of 406-kyr cycles was tuned from the depth domain to the time domain.

The evolutionary correlation coefficient (eCOCO) method was performed to track variable sedimentation rates of the studied interval (Li et al., 2018; Ma et al., 2023a). Additionally, the eCOCO analyses were conducted with the sedimentation rate varying between 1 and 20 cm/kyr using Monte Carlo simulations (2000 times). All the above analyses were conducted using Acycle v2.3 software.

4. Results

4.1. Lithofacies characteristics

Fine-grained sedimentary rock is mainly defined from the perspective of particle size of the sediments, which is widely developed in the study area. Its composition includes clay minerals, silt (quartz and feldspar), carbonate, organic matter, etc. In actual oil and gas exploration and development, it mainly refers to sedimentary rocks with relatively small particle size composed of more than two kinds of materials (the content of particles finer than 0.1 mm exceeds 50%; Aplin and Macquaker, 2011; Chen et al., 2016; Zou et al., 2014).

In recent years, some scholars have studied the lithofacies classification of the fine-grained sedimentary rocks in lacustrine basin (Chen et al., 2016; Jiang et al., 2017; Ma et al., 2022). Based on established classification schemes and the current status of oil and gas exploration and development in the study area, a classification scheme of fine-grained sedimentary rocks is proposed, taking felsic minerals (quartz plus feldspars), clay minerals and carbonate minerals as the three end-members in Fig. 3(a). XRD results indicate that there are six essential lithofacies types in the study area, which are silty limestone, calcareous mixed fine-grained sedimentary rock (CMR for short), felsic mixed fine-grained sedimentary rock (FMR for short), calcareous siltstone, clayey siltstone and siltstone. In addition, thin section identification indicates that sandstones are also present in the study area, such as fine sandstone and coarse sandstone.

Statistics show that shale oil production is closely related to TOC content (Jiang et al., 2017). Therefore, more scholars believe that the TOC content should be used in the fine-grained sedimentary rock classification (Chen et al., 2016; Hickey and Henk, 2007; Jiang et al., 2017; Ma et al., 2022). TOC content depends not only on the original productivity of organic matter, but also on preservation conditions. The deposition rate is fast and the reducibility is strong, which is conducive to the preservation of organic carbon. The original productivity is closely related to climate and nutrients, and TOC content can reflect physical and chemical conditions, not necessarily intrinsically linked to lithofacies (Jiang et al., 2017; Lu et al., 2004). Therefore, this study considers TOC content as one of the key characteristics of sedimentary environment and microfacies (lithofacies combination), rather than for lithofacies classification.

4.2. Lithofacies combination characteristics

Based on detailed core observations and sedimentological analysis in the study area, the mixed sedimentation zone is subdivided into five sedimentary microfacies: (1) calcareous semi-deep lake, (2) felsic semi-deep lake, (3) outer fan, (4) channel front, and (5) braided channel. This classification integrates lithological composition (e.g., carbonate or felsic dominance; Chen et al., 2016; Jiang et al., 2017; Ma et al., 2022), sedimentary structures (e.g., laminations, deformation features; Mulder et al., 2003), and depositional processes (e.g., turbidity currents, debris flows; Walker, 1978), following established fan-delta and

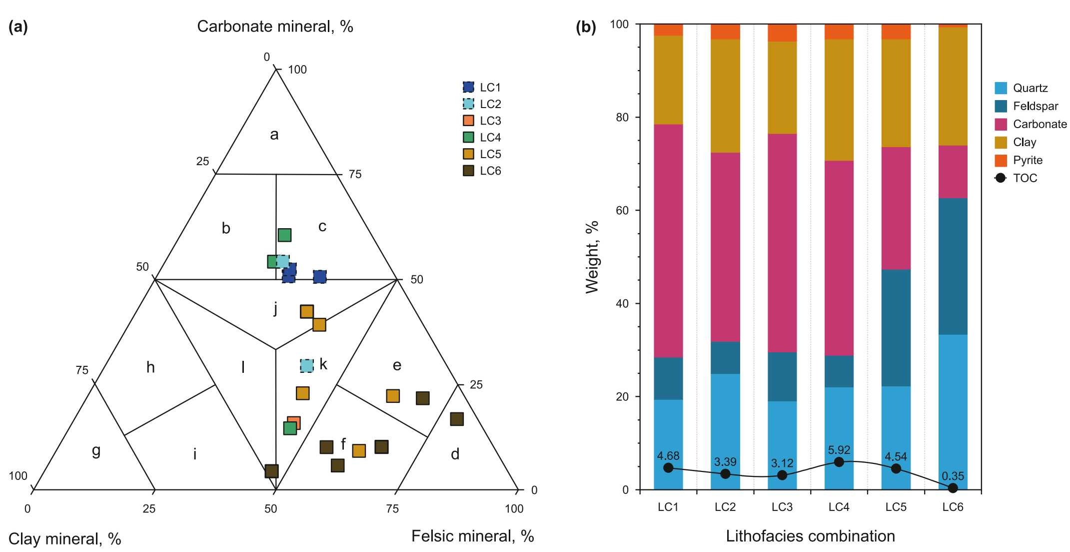

Fig. 3. Proposed classification scheme **(a)** and average composition of major minerals/TOC **(b)** for fine-grained sedimentary rocks. a. Limestone; b. Argillaceous limestone; c. Silty limestone; d. siltstone; e. Calcareous siltstone; f. Clayey siltstone; g. Claystone; h. Calcareous claystone; i. Silty claystone; j. Calcareous mixed fine-grained sedimentary rock (CMR); k. Felsic mixed fine-grained sedimentary rock (FMR); l. Argillaceous mixed fine-grained sedimentary rock (AMR); LC = Lithofacies combination.

lacustrine facies models (Cao et al., 2018; Catuneanu, 2022). The "outer fan", "channel front" and "braided channel" microfacies align with gravity flow-dominated fan systems in steep-slope basins (Mulder et al., 2003; Walker, 1978), while "calcareous/felsic semi-deep lake" microfacies reflect compositional heterogeneity in transitional lacustrine environments. The lithofacies are systematically grouped into six lithofacies combinations (LC1–LC6) based on their spatial association, sedimentary structures, and microfacies context. The lithofacies classification of the fine-grained rocks and the major mineral/TOC composition of each lithofacies combination are shown in Fig. 3. Each combination reflects distinct hydrodynamic regimes and depositional processes.

(1) Calcareous semi-deep lake microfacies is a low-energy, anoxic lacustrine environment dominated by suspension settling. LC1 is developed in this environment, characterized by laminated silty limestone, commonly containing parallel calcite veins in Fig. 4(a)–(e). The dark coloration reflects high organic matter content, indicative of a high-quality source rock (oil shale). Persistent anoxia and low hydrodynamic energy favor the preservation of organic-rich, fine-grained sediments.

(2) Felsic semi-deep lake microfacies is a quiescent lacustrine setting punctuated by episodic felsic sediment influx. LC2 is developed in this microfacies, characterized by alternating laminated silty limestone and FMR Fig. 4(f)–(i). Thin-section analysis reveals that the foresets are commonly recorded in the FMR and each foreset is separated by calcite mineral layers Fig. 4(h), signaling intermittent felsic plumes. Silty limestone mark pauses between felsic input events, with no sandstone deposition due to low-energy conditions.

(3) Outer fan microfacies is a distal fan environment influenced by dilute turbidity currents. LC3 is developed in this environment, dominated by laminated FMR, commonly containing felsic mineral layers in Fig. 5(a)–(d) (0.02–0.2 cm thick). Sedimentary structures include horizontal, deformation, and wave bedding, formed by a more dilute turbidity current in Fig. 5(a)–(d) (Cantero et al., 2012). Felsic mineral layers and absence of sandstone reflect distal, low-energy sediment gravity flows.

(4) Channel front microfacies is a proximal fan-delta zone subject to intermittent turbidity currents. LC4 and LC5 is developed in this microfacies. LC4 is made up of laminated silty limestone with interlayers of dolomitic fine sandstone in Fig. 5(e)–(g) (13.1% sandstone). LC5 is made up of laminated FMR (or CMR) with interlayers of dolomitic coarse sandstone with gravel in Fig. 5(h)–(j) (34.8% sandstone). Sedimentary structures of turbidity current deposits such as the flame structure in Fig. 6(a), incomplete Bouma sequence (graded bedding), bottom scouring surface in Figs. 5(e) and 6(b), lenticular bedding and rhythmic bedding in Figs. 5(h) and 6(c), reflecting episodic turbidity currents.

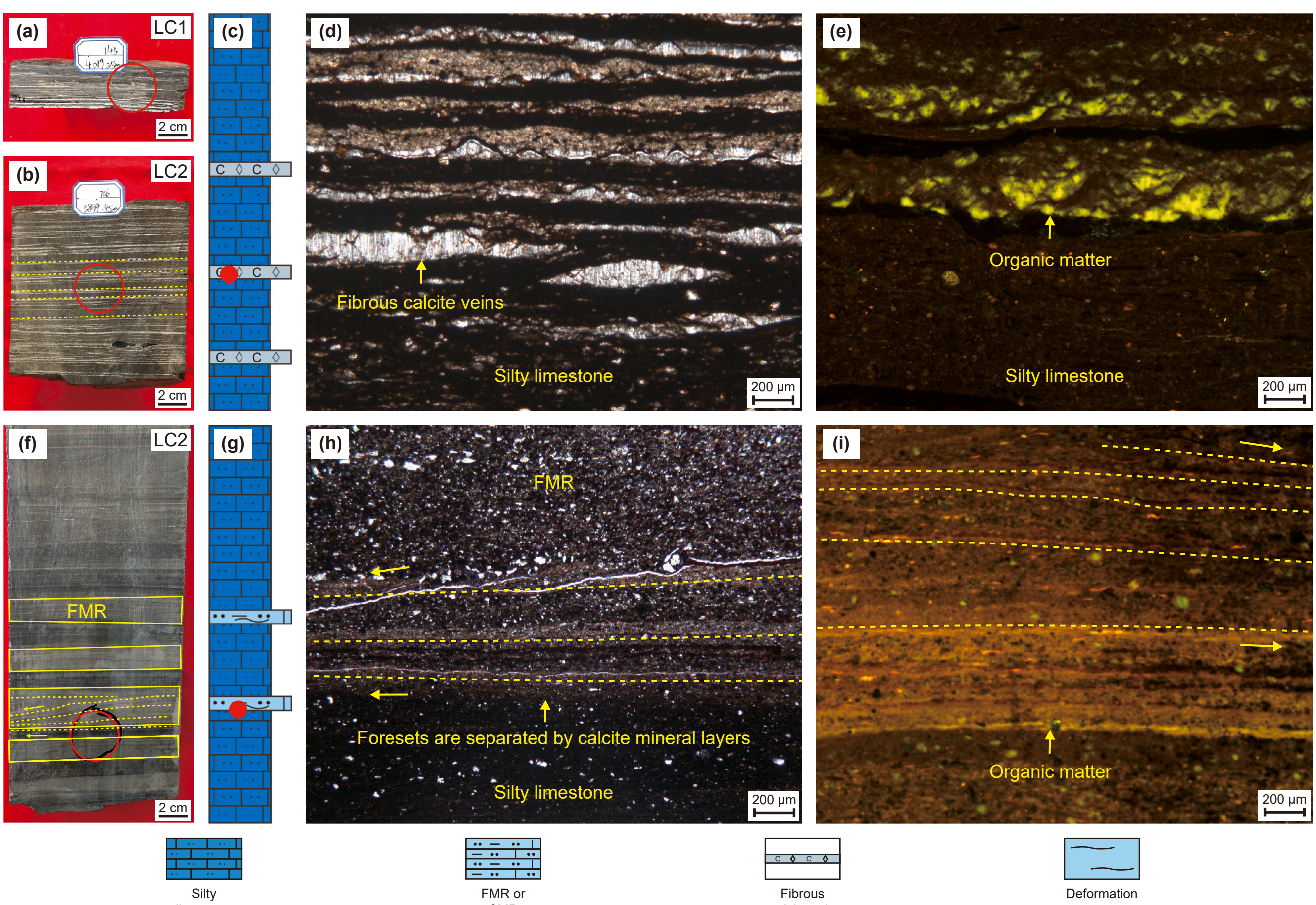

Fig. 4. Characteristics of lithofacies combinations in semi-deep lake subfacies. **(a)** The core of LC1, silty limestone with parallel calcite veins, well F143, 4019.25 m. **(b)** The core of LC1, CMR with fibrous calcite veins, well T726, 3899.45 m. **(c)** The model of LC1. **(d)** Calcite veins in the process of formation, well F143, 4019.25 m. **(e)** Fluorescence characteristics of LC1, well T726, 3899.45 m. **(f)** The core of LC 2, silty limestone and FMR with interlayers of calcite minerals, well F143, 3825.25 m. **(g)** The model of LC2. **(h)** Microscopic characteristics of LC2, well F143, 3825.25 m. **(i)** Fluorescence characteristics of LC2, well F143, 3825.25 m.

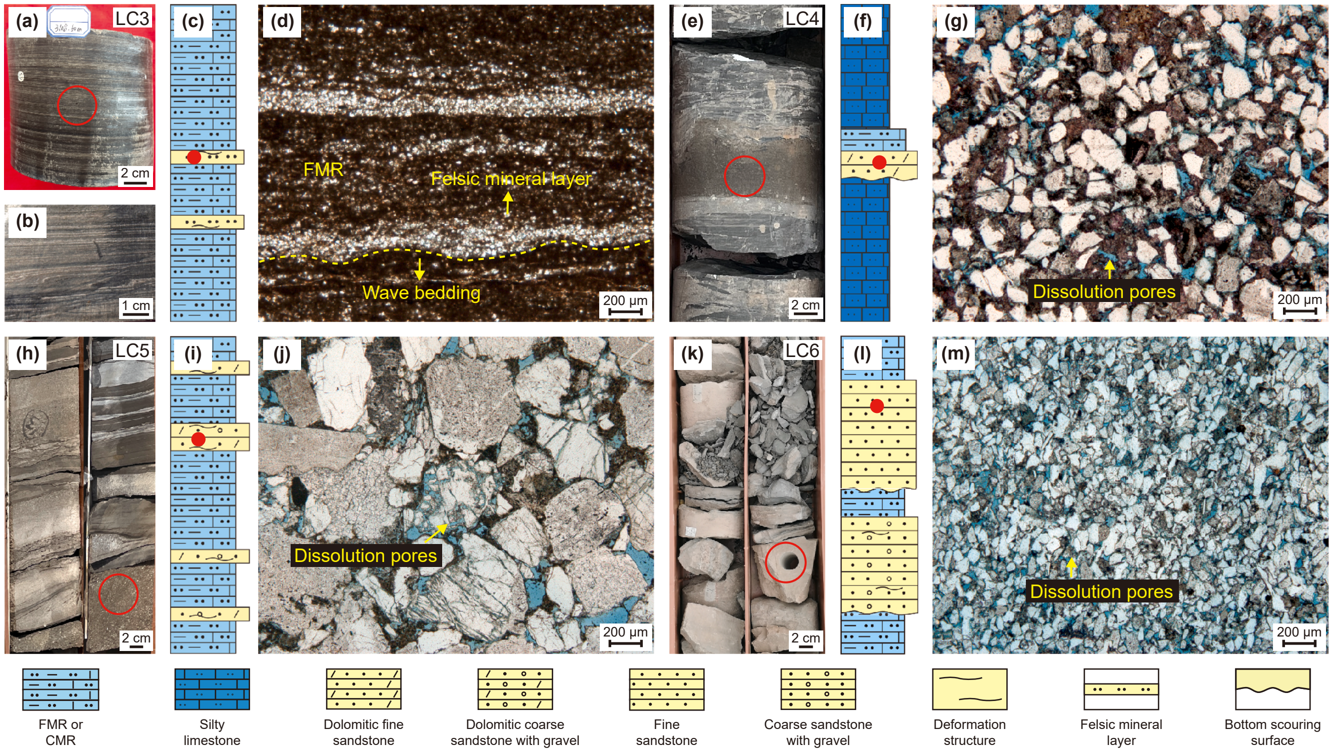

Fig. 5. Characteristics of lithofacies combinations in fan subfacies. **(a)** The core of LC3, FMR with interlayers of felsic minerals, well F112, 3108.60 m. **(b)** The core of LC3, FMR with interlayers of felsic minerals, well T729, 3272.60 m. **(c)** The model of LC3. **(d)** Microscopic characteristics of LC3, well F112, 3108.60 m. **(e)** The core of LC4, silty limestone with interlayers of dolomitic fine sandstone, well F112, 3075.20 m. **(f)** The model of LC4. **(g)** Microscopic characteristics of dolomitic fine sandstone, well F112, 3075.20 m. **(h)** The core of LC5, FMR with interlayers of dolomitic coarse sandstone with gravel, well T771, 3701.05 m. **(i)** The model of LC5. **(j)** Microscopic characteristics of dolomitic coarse sandstone with gravel, well T771, 3701.05 m. **(k)** The core of LC6, fine/coarse sandstone and FMR, well L3, 2661.30 m. **(l)** The model of LC6. **(m)** Microscopic characteristics of fine sandstone, well L3, 2661.30 m.

(5) Braided channel microfacies is a high-energy, channelized fan-delta system dominated by debris flows and turbidity currents. LC6 is usually interbedded with massive bedded fine sandstone or coarse sandstone with gravel and massive FMR (58.7% sandstone) in Fig. 5(k)–(m), with sedimentary structures of debris flow deposits such as the massive bedding in Fig. 5(k), floating torn mudstone debris in Fig. 6(d), inverse graded bedding in Fig. 6(e), and gravity sliding structure underlain the underwater collapse (twisted and disordered distributions of sandstone and fold deformation) in Fig. 6(d). These characteristics reflect syn-depositional slope instability, high-energy debris flows, and channelized gravity processes.

The lithofacies combinations are directly tied to microfacies shifts (e.g., semi-deep lake to outer fan). This hierarchical framework—from lithofacies (compositional units) to lithofacies combinations (process-driven assemblages)—clarifies how depositional dynamics govern reservoir heterogeneity.

4.3. Hydrocarbon occurrence

4.3.1. Pore types

The study on sandstone pore systems (reservoir quality) is relatively complete (Lin et al., 2024; Ma et al., 2024). The sandstone facies in the study area include two types: dissolution sandstone facies in Fig. 5(g)–(j) and (l) and cementation sandstone facies in Fig. 6(a)–(d) and (f). The appearance of dissolution sandstone facies indicates that hydrocarbons can be stored in sandstones in the channel front and braided channel microfacies (Fang et al., 2024). It is common to see organic matter (OM) filling primary pores between mineral particles and filling secondary dissolution pores in Quartz and Calcite in Fig. 7(a) by the FE-SEM studies.

However, fine-grained rocks have complex and diverse pore systems, and multiple categorizations based on pore size, shape, and accessibility have been proposed (Hu et al., 2023; Loucks et al., 2012; Ma et al., 2023b; Slatt and O'Brien, 2011; Zhang et al., 2024a). By using fluorescence microscopy, hydrocarbons mainly occur within parallel calcite veins in Fig. 4(e) and calcite mineral layers in Fig. 4(i). Based on the relationship between pores and particles (Loucks et al., 2012; Zhang et al., 2024a), there are five types of inorganic mineral pores in the study area by the FE-SEM studies in Fig. 7: (1) InterP pores (i.e., pores between mineral particles and crystals in Fig. 7(b); (2) Dissolution intraP pores (i.e., pores within particles), which are formed by the internal dissolution of mineral particles (such as dolomite) and sub-rounded to sub-angular in shape in Fig. 7(c); (3) Intraplatelet pores and interplatelet pores, which are nanoscale and mainly occur inside the I/S to form organic clay complexes in Fig. 7(d); (4) Intercrystalline pores, which are generally nanoscale and mainly occur inside pyrite framboids in Fig. 7(d); and (5) fracture pores, which are formed by the tectonic microfractures in Fig. 7(e) or formed by the bedding fractures in Fig. 7(f). The above types of pores are often filled with OM.

4.3.2. Petrophysical properties

LPNP analysis is used to measure the pore structure properties of pores with diameter less than 300 nm (Zhang et al., 2024a). The BET surface area, BJH pore volume and BJH average pore diameter before solvent extraction ranged from 0.78 to 24.65 m^2/g, 6.09–37.41 mm^3/g, and 5.70–37.28 nm (Table 2). These values

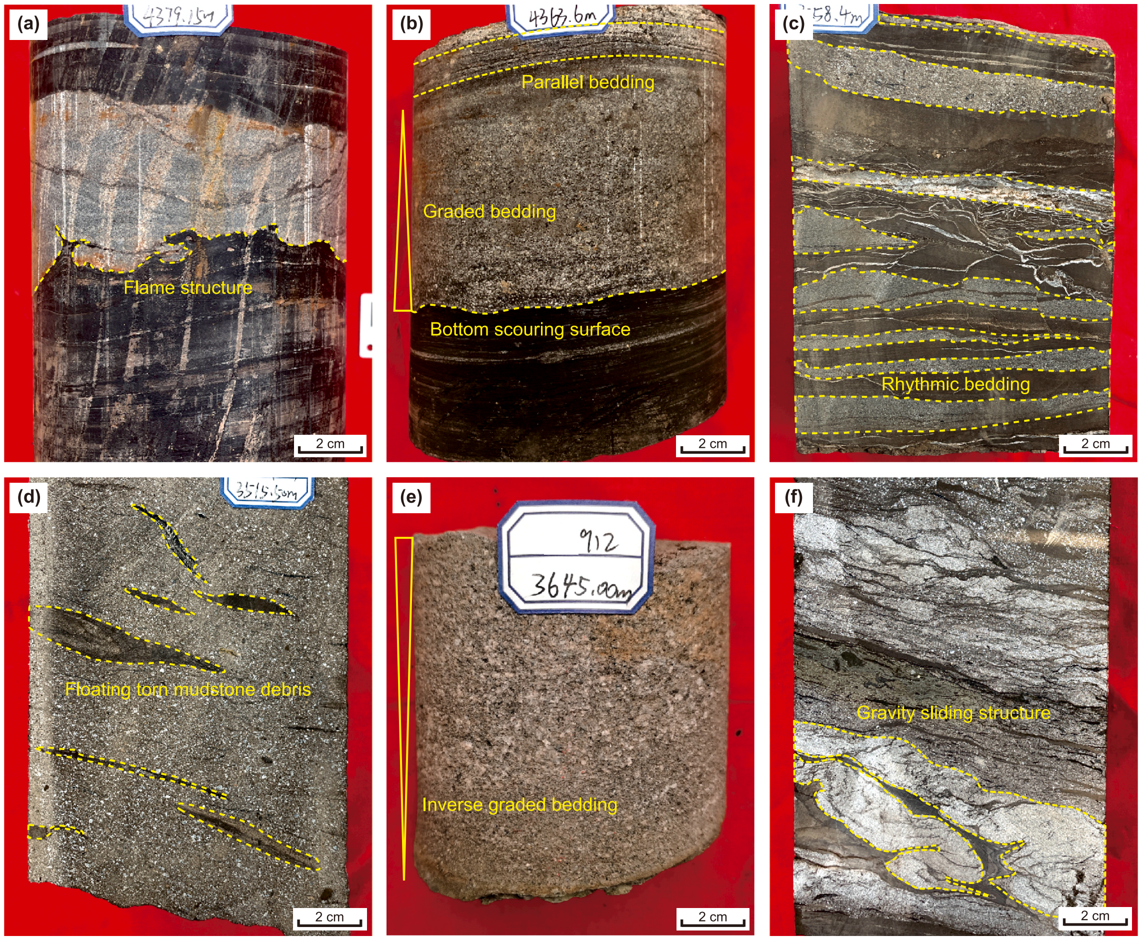

Fig. 6. Sedimentary structures in fan subfacies. **(a)** Flame structure, well T772, 4379.15 m. **(b)** Incomplete Bauma sequence (parallel and graded bedding) and bottom scouring surface, well T772, 4363.60 m. **(c)** Rhythmic bedding, well T729, 3258.40 m. **(d)** Floating torn mudstone debris, well T729, 3515.50 m. **(e)** Inverse graded bedding, well L912 3645.00 m. **(f)** Gravity sliding structure, well T771, 3831.70 m.

change to 4.95–25.57 m^2/g, 15.79–44.47 mm^3/g, and 5.61–16.16 nm after solvent extraction (Table 2). Based on the increment of BET Surface Area and BJH pore volume, the increment of LC1 and LC2 is the highest, followed by LC3, LC4 and LC5, and the increment of LC6 is the lowest (Table 2). The decrease in BJH average pore diameter may be due to the residual OM mainly being occur in pores below 10 nm.

Compared with LPNP, MIP determines a wider range of pore-throat diameter (2.8 nm–50 μm) and pore structure properties, including porosity, permeability, average pore diameter, skeletal density, bulk density and tortuosity (Zhang et al., 2024a, Table 3). The ranges of these values are 2.43%–7.68%, 0.41–12.90 mD, 8.65–13.88 nm, 2.48–2.85 g/cm^3, 2.31–2.78 g/cm^3, and 2.81–5.50, respectively (Table 3). The porosity and permeability of LC1 are both higher; LC2, LC4, LC5, and LC6 have relatively higher porosity but lower permeability; the porosity and permeability of LC3 are both lower (Table 3). The skeletal (particle) density, bulk density, and tortuosity of LC3 and LC6 are all relatively high (Table 3).

Pore morphology analysis by isothermal hysteresis loop is a common idealized method (Song et al., 2023; Zhang et al., 2024a). Fig. 8(a) and (b) show LPNP adsorption/desorption isotherms of different lithofacies combinations before and after solvent extraction. At higher pressure, the adsorption and desorption isotherms do not overlap, and there are hysteresis loops. Isothermal hysteresis loop is similar to H3 and H4 types in the IUPAC classification (Sing, 1985; Zhang et al., 2024a), indicating that the pores of these six lithofacies combinations are slit-shaped pores and narrow slit-like pores, and the pores of LC3 are mostly slit-shaped pores in Fig. 8(a). There was no significant change in isothermal adsorption before and after solvent extraction in Fig. 8(b), which confirmed that the pores containing OM are the above-mentioned pores. When the relative pressure is greater than 0.9, the adsorption of N_2 increases rapidly, indicating that the presence of macropores (>50 nm) has a significant contribution to the total pore volume (Zhang et al., 2024a).

For the pore size distribution plot of LPNP results after solvent extraction in Fig. 8(c), the vertical coordinate is dV/dlog$D$, which eliminates the influence of the number of data points on the pore size distribution and highlights the existence of relatively large diameter pores (Liu and Ostadhassan, 2019; Zhang et al., 2024a). The pore size distribution has two peaks, one at 2–10 nm and the other at 20–30 nm in Fig. 8(c). For the plot of the incremental pore size distribution after solvent extraction of the LPNP results, the vertical coordinate is dΔV/dlog$D$. Residual OM exists in pores between 2 and 30 nm, mainly in pores below 10 nm, followed by pores between 10 and 30 nm in Fig. 8(d).

The mercury intrusion and extrusion curves in MIP tests are shown in Fig. 9(a). Under low pressure, the intrusion volume of mercury increases slowly with the increase of pressure. However, when the intrusion pressure is greater than 10 MPa, the intrusion volume of mercury increases rapidly, accounting for more than half of the total volume, indicating the existence of nanoscale pores (Hu et al., 2017; Kuila and Prasad, 2013; Zhang et al., 2024a). The obvious hysteresis in the mercury extrusion curve indicates

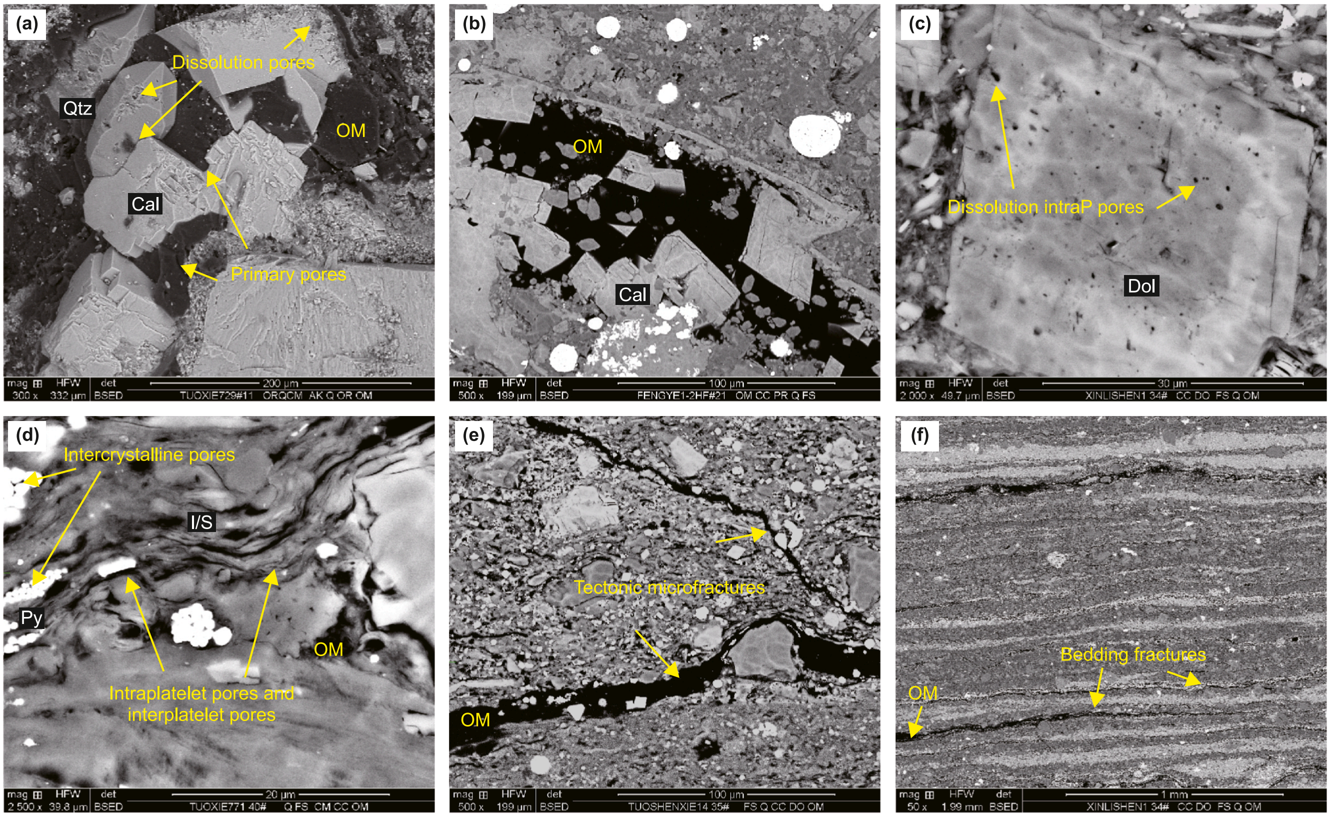

Fig. 7. FE-SEM images of different types of pores. **(a)** Primary pores and secondary dissolution pores, Coarse sandstone, well T729, 3515.5. **(b)** InterP pores between carbonate mineral particles, FMR, well F1-2, 3831.30 m. **(c)** Dissolution intraP pores formed by the internal dissolution of dolomite, Silty limestone, well X1, 4381.00 m. **(d)** Intraplatelet pores and interplatelet pores inside the I/S, Intercrystalline pores inside the pyrite framboids; Clayey siltstone, well T771, 3800.89 m. **(e)** Fracture pores formed by the tectonic microfractures, FMR, well T14, 3767.85 m. **(f)** Fracture pores formed by the bedding fractures, Silty limestone, well X1, 4381.00 m; OM = organic matter; Qtz = quartz; Cal = calcite; Dol = dolomite. I/S = mixed illite-smectite; Py = pyrite; InterP pores = pores between mineral particles and crystals; IntraP pores = pores within particles.

Table 2
Pore structure parameters for fine-grained rocks of six lithofacies combinations based on LPNP analyses and solvent extraction comparison.

Lithofacies combination	Before solvent extraction			After solvent extraction					
	BET surface area, m^2/g	BJH pore volume, mm^3/g	BJH average pore diameter, nm	BET surface area, m^2/g	BJH pore volume, mm^3/g	BJH average pore diameter, nm	Incremental BET surface area, m^2/g	Incremental BJH pore volume, mm^3/g	Incremental BJH average pore diameter, nm
LC1	6.57	20.03	10.90	16.33	30.11	7.65	9.77	10.08	−3.25
LC2	1.92	11.10	25.22	15.55	28.64	9.14	13.63	17.54	−16.07
LC3	12.89	37.41	10.85	23.64	44.47	8.50	10.75	7.06	−2.35
LC4	0.78	6.09	37.28	4.95	15.79	16.16	4.16	9.70	−21.12
LC5	4.83	15.53	12.38	10.16	21.79	9.68	5.33	6.25	−2.70
LC6	24.65	28.05	5.70	25.57	27.39	5.61	0.92	−0.66	−0.09

Notes: LC1 (Well F143, 4019.20 m); LC2 (Well F143, 3825.25 m); LC3 (Well T729, 3272.60 m); LC4 (Well F112, 3075.30 m); LC5 (Well T771, 3800.89 m); LC6 (Well L89, 3451.35 m).

Table 3
Pore structure parameters for fine-grained rocks of six lithofacies combinations from MIP analyses.

Lithofacies combination	Porosity, %	Permeability, mD	Average pore diameter, nm	Skeletal density, $/cm^3$	Bulk density, g/cm^3	Tortuosity	Pore volume at different connected networks, mm^3/g						
							2.8–5 nm	5–10 nm	10–50 nm	50–100 nm	0.1–1 μm	1–10 μm	10–50 μm
LC1	6.80	12.90	13.88	2.51	2.34	2.81	2.57	10.80	7.37	1.29	2.33	2.62	2.11
LC2	6.96	2.36	11.87	2.48	2.31	4.21	3.52	11.36	9.53	1.70	1.54	1.77	0.76
LC3	2.43	0.41	9.69	2.85	2.78	5.39	1.31	4.90	1.13	0.22	0.56	0.45	0.16
LC4	4.41	1.64	9.45	2.59	2.48	3.80	4.24	5.42	4.99	1.28	0.75	0.77	0.33
LC5	5.27	3.43	11.00	2.71	2.56	3.78	2.63	10.13	4.05	0.54	1.30	1.24	0.67
LC6	7.68	2.03	8.65	2.76	2.55	5.50	7.66	13.10	2.58	0.55	1.23	4.19	0.84

Notes: LC1 (Well T729, 3899.45 m); LC2 (Well F143, 3825.25 m); LC3 (Well X1, 4377.40 m); LC4 (Well F112, 3075.30 m); LC5 (Well F1-2, 3831.30 m); LC6 (Well L89, 3451.35 m).

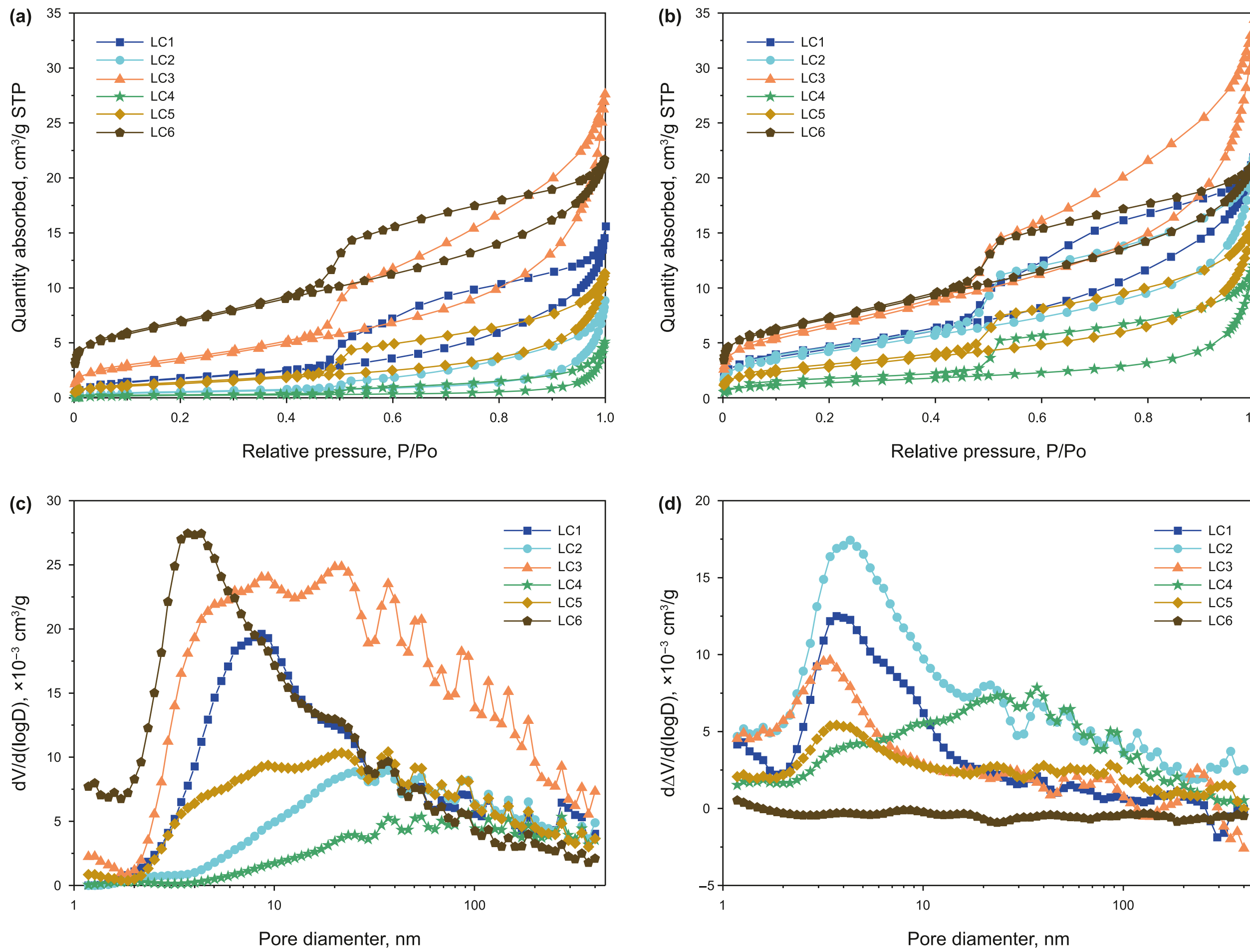

Fig. 8. LPNP results of fine-grained sedimentary rock with different lithofacies combinations. **(a)** Adsorption and desorption isotherms before solvent extraction. **(b)** Adsorption and desorption isotherms after solvent extraction. **(c)** Pore size distributions after solvent extraction, with the vertical coordinates d*V*/d(log*D*) (*V*: pore volume; *D*: pore diameter). **(d)** Incremental pore size distributions after solvent extraction, with the vertical coordinates dΔ*V*/d(log*D*) (Δ*V*: incremental pore volume generated by extraction; *D*: pore diameter).

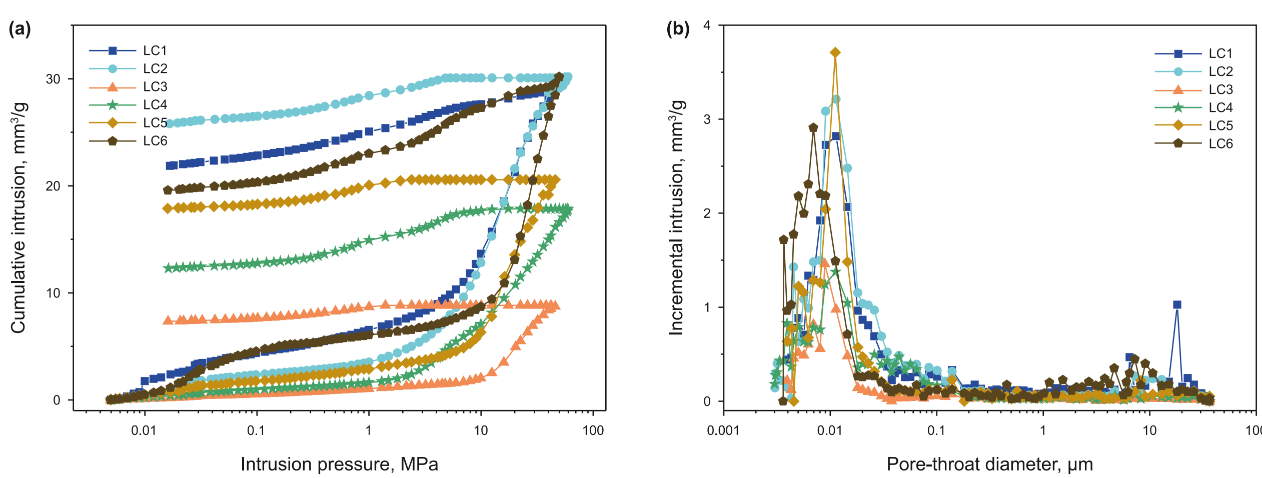

Fig. 9. MIP results of fine-grained sedimentary rock with different lithofacies combinations. **(a)** Intrusion/extrusion curves of MIP. **(b)** Pore-throat size distribution.

that the connectivity of the pore network in LC2 – LC5 is poor (Zhang et al., 2024a).

The pore size distribution obtained by MIP tests has a clear main peak and a smaller secondary peak in Fig. 9(b). The main peaks are in the range of nanoscale pore-throat size (2.8–400 nm), and the small secondary peaks are in the range of pore-throat size greater than 4 μm, which may be related to the presence of microfractures in these samples in Fig. 7(e) (Zhang et al., 2024a). Table 3 shows that the pore-throat size is mainly within the range of 5–50 nm in LC1, LC2, LC4 and LC5, and 2.8–10 nm in LC3 and LC6.

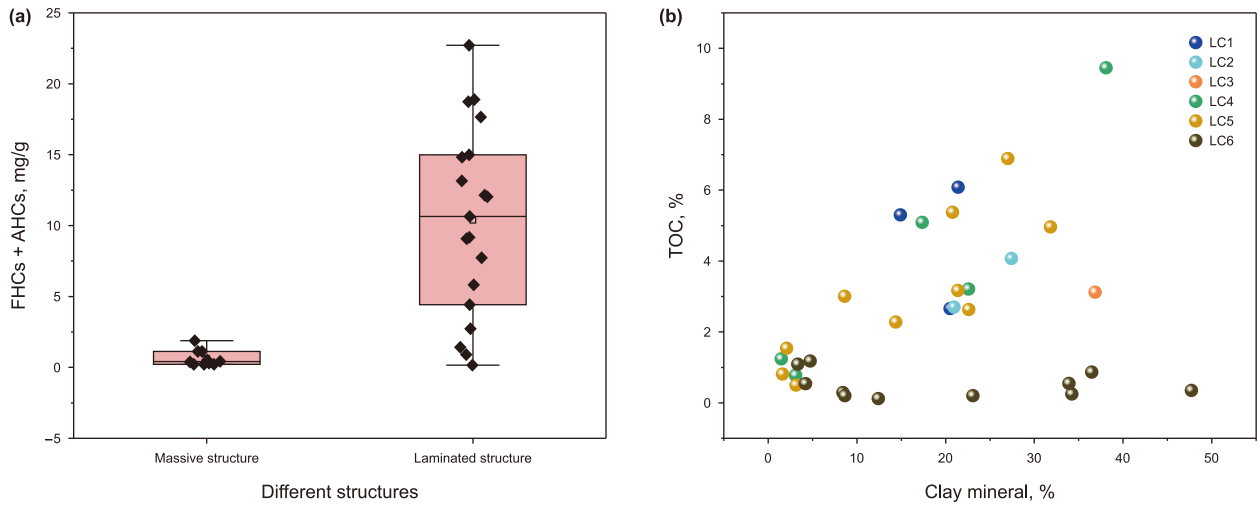

Fig. 10. XRD, TOC and SBS Rock-Eval pyrolysis analysis results of different structures **(a)** and different lithofacies combinations **(b)**.

Table 4
Thickness weighted calculation results of petrophysical/OM properties for each lithofacies combination.

Lithofacies combinations	Sedimentary microfacies	Porosity, %	TOC, %	T_{max}, °C	FHCs, mg/g	AHCs, mg/g
LC1	Calcareous semi-deep lake	5.12	4.68	445.33	6.64	4.68
LC2	Felsic semi-deep lake	2.26	2.78	442.65	5.00	4.66
LC3	Outer fan	0.22	2.64	437.50	1.34	1.40
LC4	Channel front	5.03	5.84	438.79	5.53	10.81
LC5	Channel front	6.38	3.23	440.63	6.11	3.98
LC6	Braided channel	5.30	0.53	427.28	1.08	0.53

Notes: FHCs = free hydrocarbons; AHCs = adsorbed hydrocarbons.

4.4. OM properties of lithofacies combinations

The abundances of OM in fine-grained sedimentary rocks among the six lithofacies combinations are significantly different in Fig. 3(b). And the content of OM in laminated shale was much higher than in massive shale in Fig. 10(a). Moreover, there is a rule that the OM content increases with the increase of clay mineral content in Fig. 10(b), which may be due to the OM content in the organic clay complexes was high in Fig. 7(d) (Hou et al., 2023). However, this rule does not apply in LC6 in Fig. 10(b), suggesting that clay minerals with high surface area (Table 2) in the high-energy braided channel microfacies may primarily host pore water rather than hydrocarbons. Similar observations in nearshore marginal lacustrine facies have been attributed to rapid sedimentation and limited organic-clay interactions under dynamic hydrodynamic conditions (Gorynski et al., 2019; Li et al., 2019a; Zhao et al., 2023).

An innovative methodology was developed to study OM properties based on lithofacies combinations from the perspective of mathematical weighted average. According to statistical principles, the comprehensive OM properties of lithofacies combinations are obtained by calculating the thickness-weighted average of OM parameters of different lithofacies. The principle of its calculation formula is as follows:

$$N = \frac{d_1}{\sum_{i=1}^{n} d_i} N_1 + \frac{d_2}{\sum_{i=1}^{n} d_i} N_2 + \frac{d_3}{\sum_{i=1}^{n} d_i} N_3 + \ldots + \frac{d_n}{\sum_{i=1}^{n} d_i} N_n$$

Notes: The N_n is the average quantitative parameter of the nth lithofacies within a lithofacies combination; the d_n is the total thickness of the nth lithofacies within a lithofacies combination; the N is the comprehensive OM parameters of the lithofacies combination. The thickness-weighted average method is also applicable to the analysis of petrophysical properties.

Calculation results from MIP, TOC and SBS Rock-Eval pyrolysis analysis are shown in Table 4. For the six lithofacies combinations, calculated average porosity falls between 0.22% and 6.38%; TOC varies from 0.53% to 5.84%; T_{max} ranges from 427.28 to 445.33 °C, indicating that most of the LCs are in the early mature stage. FHCs are in the range of 1.08–6.64 mg HC/g rock, and AHCs values vary from 0.53 to 10.81 mg HC/g rock, indicating that LC1, LC2, LC4 and LC5 have higher hydrocarbon content and LC3 and LC6 shows poor hydrocarbon content (Table 4).

4.5. Geological response to astronomical cycles

To assess astronomical forcing mechanisms, we first generated the power spectrum of the ETP theoretical series spanning 39.2–44.4 Ma (Fig. 2) using the La2010d orbital solution (Laskar et al., 2004, 2011; Wang et al., 2020b). This analysis quantified the theoretical astronomical period ratios as 406: 127: 97: 40: 23: 19 for the studied interval. The 2π MTM power spectra shows that the corresponding ratio of the 6 peaks is 406: 127.2: 96.6: 39.9: 22.9: 18.9 in Fig. 11(a), which is almost consistent with the theoretical astronomical period ratio. The corresponding depth-domain thicknesses for these cycles are 30.18 m: 9.45 m: 7.17 m: 2.96 m: 1.70 m: 1.41 m. And the 406-kyr long eccentricity cycle, exhibiting the highest spectral power in Fig. 11(a), is interpreted as the dominant orbital control on sedimentary cyclicity in the study area (Huang and Hinnov, 2019; Ma et al., 2023a; Shi et al., 2020). The eCOCO analyses indicate a likely mean sediment accumulation rate of ~7.6 cm/kyr for the studied

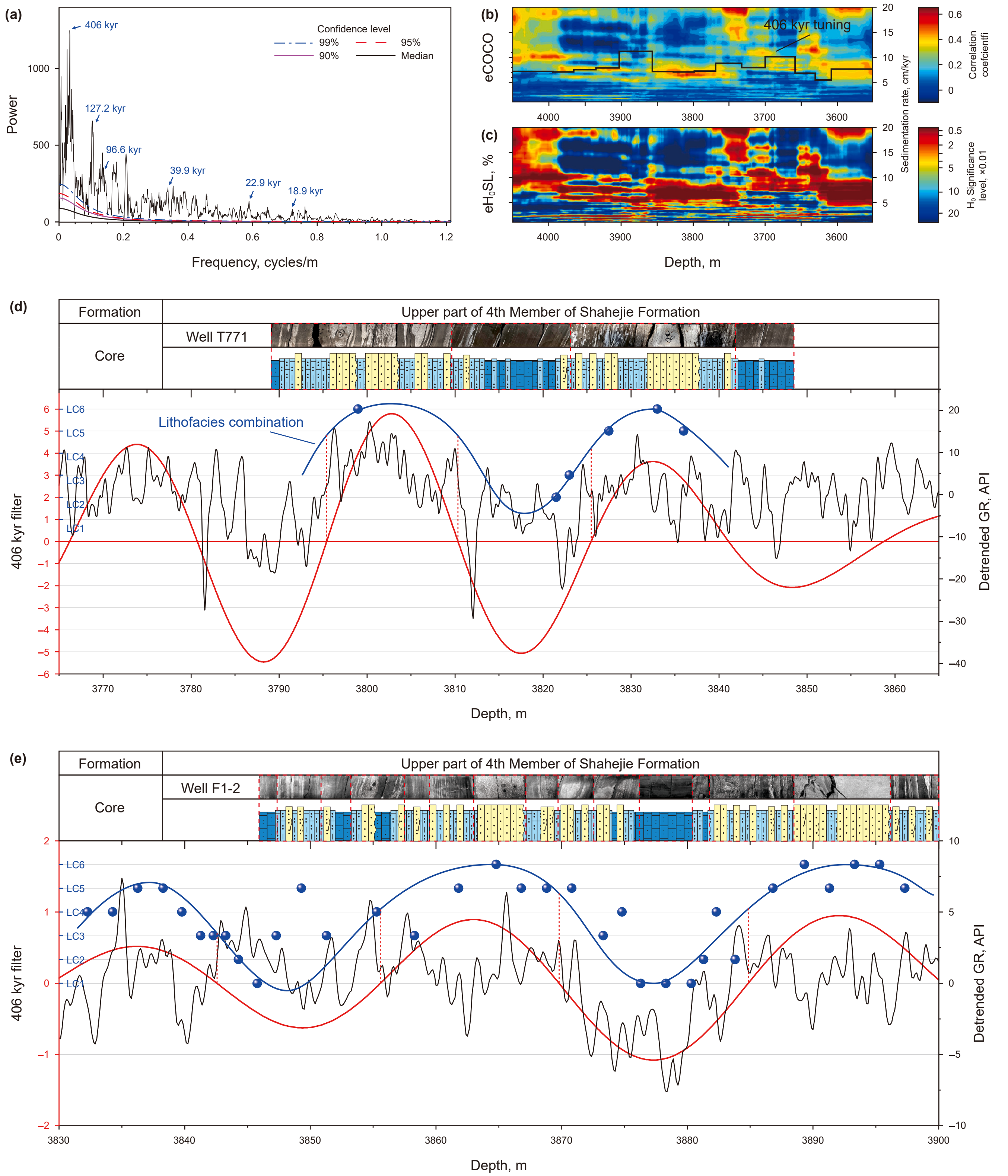

Fig. 11. Interpreted cyclostratigraphy of Es4s of well T771 and well F1-2. (a) The 2π MTM power spectra of detrended gamma ray data depth (3500–4100 m). Results of evolutionary correlation coefficient (eCOCO) analyses **(b)**, the sedimentation rate curve (black line) based on 406-kyr tuning and evolutionary null hypothesis (H_0) significance level **(c)** of the gamma ray series. The relationship between event sedimentation and filtered cycles. Detrended gamma ray (black line) of cored interval of well T771 **(d)** and well F1-2 **(e)** are Gaussian filtered (red line) for ~30.18 m cycles (0.033 $\pm$ 0.007 cycles/m). The filtered cycles are interpreted as 406-kyr cycles. The lithofacies combination division results (blue line connecting the median depth of each lithofacies combinations) are based on cores observation of well T771.

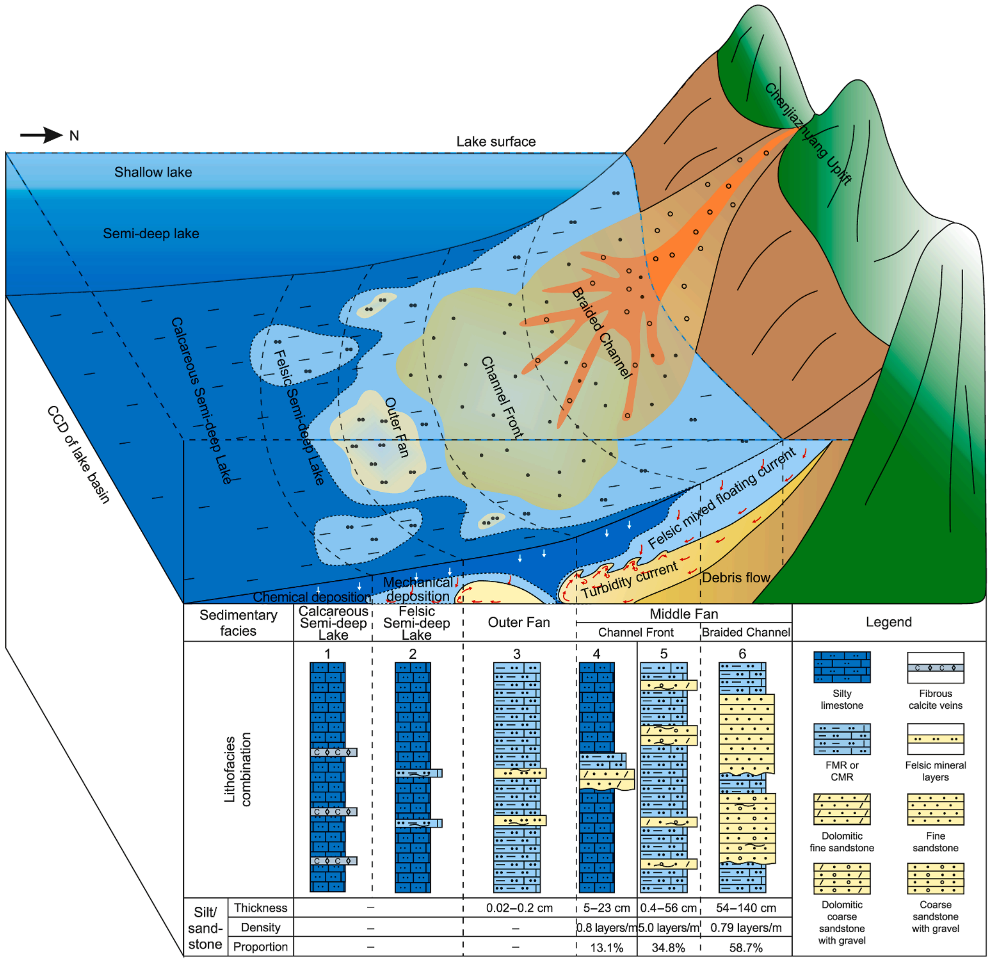

Fig. 12. The depositional model for mixed sedimentation zone in the northern steep slope zone of the Dongying Sag.

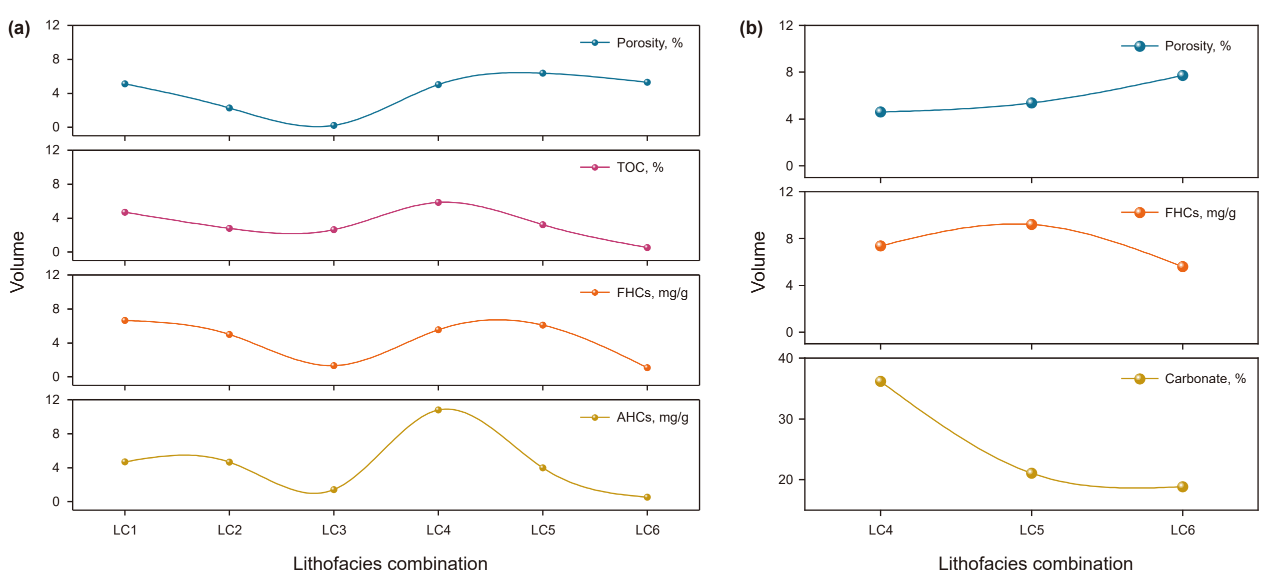

Fig. 13. Comparison of comprehensive properties **(a)** and sandstone properties **(b)** for each lithofacies combination (Table 4).

interval in Fig. 11(b) and (c), which is consistent with the value of 7.5–11.0 cm/kyr obtained by previous studies (Xu et al., 2023). After the above analysis, a suitable and reliable Milankovitch cycle curve can be obtained through filtering in Fig. 11(d) and (e). The sedimentation rate curve in Fig. 11(b) (black line) based on 406-kyr age tuning of the longest statistically significant cycles in the data in Fig. 11(a) confirms the accuracy of the 406-kyr filter in Fig. 11(d) and (e).

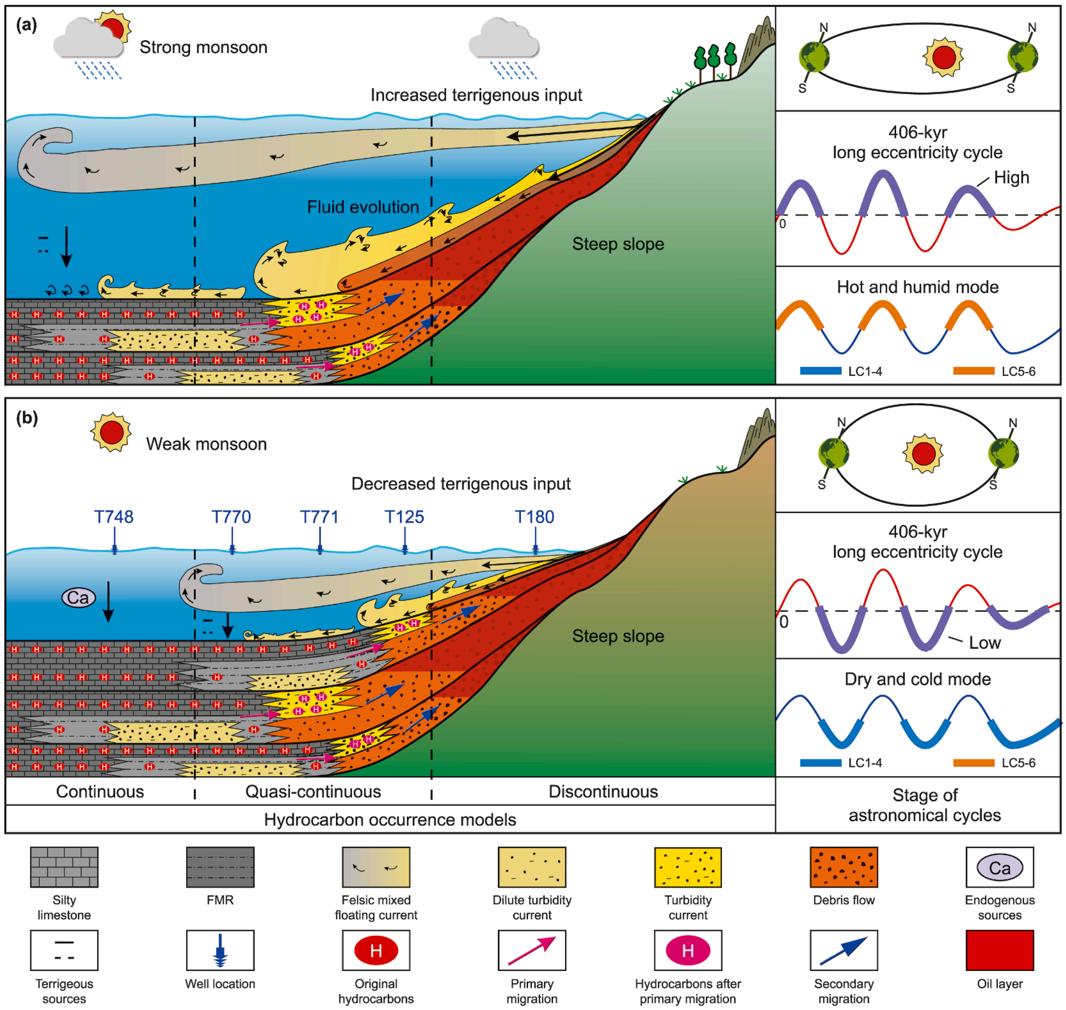

Fig. 14. Sedimentary evolution and hydrocarbon occurrence model for transition zone between conventional and unconventional hydrocarbon reservoirs controlled by high **(a)** and low **(b)** 406-kyr long eccentricity cycles for mixed sedimentation zone in the Northern Steep slope zone of the Dongying Sag (modified from Shi et al., 2020; Xu et al., 2023; Zhang et al., 2024b). The data in the lithological profile are derived from well-to-well correlation, with the well locations illustrated in Fig. 1(a).

The identification result of lithofacies combinations in well T771 in Fig. 11(d) and (e) indicate that the 406-kyr long eccentricity cycle modulates sandstone-mudstone alternations in the northern steep slope zone: high long eccentricity phases (406-kyr maxima) correlate with thick sandstone units (LC5–LC6), while low phases correspond to mudstone-dominated lithofacies (LC1–LC4) in Fig. 11(d) and (e). The integrated evolution of sandstone and mudstone (i.e. lithofacies combination) based on astronomical cycle theory analysis has shown a clear regularity in the mixed sedimentation zone in the northern steep slope zone of Dongying Sag.

5. Discussion

5.1. Depositional model

Based on the comparison of ancient and modern fine-grained sediments, it is found that as the water depth increases from the lake basin edge towards the center of the basin, the content and particle size of quartz and feldspar decrease due to sedimentary differentiation in Fig. 3(b) (Cao et al., 2018). And OM is adsorbed onto clay minerals and its content gradually increases in Fig. 10(b), but the occurrence of deep-water slope gravity-flow deposits may lead to a regional decrease of OM content in the vicinity of the basin center in Fig. 3(b) (LC3). Studies on the influence of mineral and OM composition on particle density have shown that a decrease in OM content and an increase in clay mineral content indicate an increase in particle density (Joerg and Martin, 2020; Robinson et al., 2022). LC3 exhibits particle and bulk densities comparable to LC6 (FMR), indicating that it is caused by the enrichment of terrigenous organic-lean clay minerals carried by turbidity currents. Based on the lithofacies classification of XRD data, the fluid that forms FMR carried by deep-water gravity flow is defined as the felsic mixed floating current in this study, which is the hypopycnal plume for floating river water that has lower density than basin water (Bates, 1953; Shanmugam, 2018). Felsic mixed floating current extends as far as felsic semi-deep lake and appears as thin layers in LC2 in Fig. 4(f). The fine-grained sedimentary rock of LC4 are mainly composed of silty limestone, indicating that LC4 is almost unaffected by felsic mixed floating current, while the fine-grained rock of LC5 and LC6 is FMR, indicating that there is a gap of the felsic mixed floating current at LC4.

A depositional model was further established in order to clearly describe the sedimentary process for the mixed sedimentation zone in the northern steep slope zone of the Dongying Sag (Fig. 12). As the water depth decreases from the center of the basin towards the lake basin edge, there are five microfacies: calcareous semi-deep lake (LC1), felsic semi-deep lake (LC2), outer fan (LC3), channel front (LC4 and LC5) and braided channel (LC6) in the middle fan.

(1) In calcareous semi-deep lake above the CCD where the rate of supply of calcium carbonate is greater than the rate of dissolution, the minerals are mainly carbonate and clay. The reducibility of lake water results in the higher OM content in Fig. 13(a). Controlled by chemical deposition caused by biological forces and seasonal stratification of the lake water (Fig. 12), LC1 developed horizontal laminated organic-rich silty limestone containing parallel calcite veins in Fig. 4(a)–(e) (Bai et al., 2018). And hydrocarbon generation processes likely induced the formation of bedding-parallel calcite veins of fibrous sparry calcite through recrystallization from sedimentary layers in Fig. 4(d) (Zhang et al., 2016).
(2) In felsic semi-deep lake, interbedded FMC developed on the basis of silty limestone in the calcareous semi-deep lake (LC1) due to the influence of the felsic mixed floating current (Fig. 12). As a result of the low supply of OM and difficulty in preservation in the felsic mixed floating current, the OM content in LC2 is lower than that in LC1 in Fig. 13(a). During the transportation of fine-grade felsic particles by felsic mixed floating current from north to south in the northern steep slope zone of the Dongying Sag, fine-grade felsic particles are prone to form foresets within the bottom currents. Lateral migration and frontal progradation of foresets under the action of bottom currents results in multiple stacked and laterally-connected foresets in Fig. 4(h) and (i), ultimately controlling the accumulation and preservation sites of the FMR (Cao et al., 2024).
(3) In outer fan, the basis lithofacies has completely changed to the laminated FMR controlled by the felsic mixed floating current, resulting in LC3 becoming a key lithofacies combination for the accumulation of terrigenous organic-lean clay minerals. Due to the influence of terrigenous fine-grained debris under the suspended load of dilute turbidity currents (Fig. 12) and hydrodynamic conditions, FMR are formed with deformation bedding in Fig. 5(b), and wave bedding in Figs. 5(d) and 12. The physical and OM properties of LC3 are inferior to those of LC1 and LC2, but the TOC content is still more than 2% in Fig. 13(a).
(4) In channel front of the middle fan, LC4 has not been significantly affected by felsic mixed floating current, and the basis lithofacies remains silty limestone. But LC4 has fine sandstone interlayers with a thickness of 5–23 cm affected by turbidity currents, and dissolution pores are developed in sandstone in Figs. 6(g) and 12. The small amount of felsic mixed floating current carried by the turbidity current can control the formation of thin interlayers of FMR beside the sandstone in Figs. 5(e)–(g) and 12. As the hydrodynamic force increased significantly, LC5 are controlled by turbidity current and felsic mixed floating current, resulting in the development of coarse sandstone interlayers with a thickness of 0.4–56.0 cm on the basis of FMR in Figs. 5(h) and 12. At the same time, the content of terrigenous felsic minerals in the fine-grained sediments developed in LC5 has also significantly increased in Fig. 3(b), which may have led to the improved physical properties (porosity, permeability, and pore diameter) of fine-grained sediments in Table 3 and Fig. 8(c). The thermal evolution of OM in organic-rich silty limestone and FMR can produce plenty of organic acids (Dutton, 2008). These acids can partially dissolve unstable minerals in sandstones such as feldspar, forming a large number of secondary dissolution pores in LC4–LC5 in Fig. 6(g) and (j) (Fang et al., 2024). In summary, the OM properties and physical properties of LC4 and LC5 are superior to those of LC3 in Fig. 13(a).
(5) In underwater braided channel of the middle fan, the LC6 consists of interbedded massive bedded (0.54–1.40 m) fine sandstone or coarse sandstone with gravel and FMR (Fig. 12). Sediments are mainly supplied by debris flows, tractive currents generated by normal mountain-derived river discharges during non-flood periods, and fine-grained suspension sedimentation (Cao et al., 2018). Controlled by the weakest deep lake influence and the strongest terrigenous input influence, LC6 becomes a key lithofacies combination for the accumulation of terrigenous felsic minerals in Fig. 3(b). Therefore, fine-grained sediments of LC6 have the worst OM properties but the highest porosity among the six lithofacies combinations in Fig. 3(b) and Table 3. As the thickness of the sandstones increases, the average content of carbonate cements gradually decreases from LC4 to LC6, resulting in a gradual increase in porosity in Fig. 13(b). Diagenesis plays a decisive role in this process, as thinner sandstones are often more easily cemented (Fang et al., 2024). Hydrocarbons can migrate from semi-deep lake to braided channel through faults, bedding, and other mechanisms. Under the control of formation pressure and oil-water displacement (buoyancy), hydrocarbons can migrate again towards higher positions within the braided channel sandstones (Pranter and Sommer, 2011). On the whole, LC6 has high porosity, but poor OM properties in Fig. 13(a) and (b).

5.2. Sedimentary evolution and hydrocarbon occurrence model

Orbital forcing exerts first-order controls on sedimentary evolution through modulation of paleoclimate dynamics at both global and regional scales. During the Eocene greenhouse climate, orbital parameters (eccentricity, obliquity, precession) exerted latitude-dependent controls on solar radiation distribution, atmospheric circulation, and monsoon intensity (Licht et al., 2014; Westerhold et al., 2020; Zhao et al., 2025). While prior studies emphasize the role of long obliquity (1.2 Ma) in regulating low-latitude lake-level fluctuations and organic matter burial at million-year scales (Zhao et al., 2025), our work highlights the dominance of the 406-kyr eccentricity cycle in controlling meter-scale lithofacies heterogeneity. This distinction aligns with global frameworks where eccentricity dominates low-latitude hydroclimate under greenhouse conditions, as obliquity signals weaken without polar ice sheets to amplify their effects (Westerhold et al., 2020). Specifically, the 406-kyr cycle amplified seasonal contrasts in East Asia, driving monsoon intensification and pulsed sediment delivery to the Dongying Sag (Huang and Hinnov, 2019; Liu et al., 2018; Ma et al., 2023a; Shi et al., 2020; Wang et al., 2020b; Wei et al., 2024a; Xu et al., 2023; Zhang et al., 2024b). High eccentricity phases enhanced terrigenous input, forming sandstone-rich lithofacies (LC5–LC6), while low phases favored organic-rich shales (LC1–LC4). These findings bridge latitudinal climate dynamics with basin-scale sedimentation processes, resolving how orbital forcing cascades from global insolation gradients to lithofacies combination-scale heterogene. Differences in lithofacies combinations govern source-reservoir assemblage characteristics and hydrocarbon distribution, which affect the development methods and engineering processes of the conventional reservoirs and unconventional reservoirs (Guo et al., 2023; Hu et al., 2024; Shen et al., 2021). After summarizing the above process and completing well-to-well correlation (T748, T770, T771, T125 and T180 in Fig. 1(a)), a sedimentary evolution and hydrocarbon occurrence model of ordered coexistence of source and reservoir is established for mixed sedimentation zone in the northern steep slope zone of the Dongying Sag (Fig. 14).

During high eccentricity phases, increased solar radiation enhanced latitudinal thermal gradients, strengthening the East Asian monsoon (Xu et al., 2023). Warm-humid conditions intensified seasonal rainfall, triggering frequent floods and hyperpycnal flows. These processes delivered coarse-grained sediments (e.g., LC5–LC6 lithofacies) via debris flows and turbidity currents, while high-energy conditions diluted organic carbon preservation in fine-grained sediments in Figs. 3(b) and 14(a).

During low eccentricity phases, reduced solar radiation at perihelion led to drier climates with weakened monsoons (Xu et al., 2023). Limited rainfall stabilized sediment supply, favoring suspension settling of clay and organic matter (LC1–LC4 in Fig. 14(b)). However, episodic hyperpycnal flows during lake-level lowstands deposited isolated sandstone interlayers in Fig. 5(e), while slope instability under low hydrodynamic energy promoted slump and turbidite deposition (Xu et al., 2023). These conditions enhanced organic carbon accumulation in laminated shales (LC1–LC4 in Fig. 3(b)), contrasting with high-energy phases.

Under the combined action of structural location and gravity flow distribution controlled by the long eccentricity cycle, the ordered coexistence of conventional and unconventional reservoirs has been formed in the study area. Based on the differences in hydrocarbon occurrence characteristics of different lithofacies combinations and source-reservoir assemblage types of different sedimentary microfacies controlled by astronomical cycles, three hydrocarbon occurrence models are identified: (1) continuous ("united source-reservoir"), (2) quasi-continuous ("adjacent source-reservoir"), and (3) discontinuous ("separated source-reservoir") hydrocarbon accumulations (Fig. 14).

(1) Continuous hydrocarbon accumulation

Continuous hydrocarbon accumulation refers to unconventional oil and gas resources accumulated within source rocks (Li et al., 2015). Due to the fact that the source rock is both a source rock and a reservoir, it can also be referred to as "shale oil and gas". Controlled by organic-rich shale, continuous hydrocarbon accumulation mainly developed in the semi-deep lake and outer fan microfacies (LC1–LC3). Hydrocarbons remain *in situ* in clay mineral layers with high OM content (organic clay complexes, Fig. 7(d)), or undergo micro-migration from organic rich layers to adjacent calcite veins and calcite mineral layers in Figs. 4(e), (i) and 10. Inorganic pores, particularly recrystallization intercrystalline pores in calcite developed in the laminations in Fig. 10(a), are the key matrix pores for lacustrine shale oil (Fig. 7(b); Liang et al., 2022). Recent advances in micro-migration characterization (e.g., Hu et al., 2024; Pan et al., 2023; Yuan et al., 2025) provide new insights into differential enrichment mechanisms of shale oil.

(2) Quasi-continuous hydrocarbon accumulation

Quasi-continuous hydrocarbon accumulation refers to unconventional oil and gas resources accumulated in tight reservoirs that are in close contact with organic-rich source rocks, also known as "tight oil and gas". After hydrocarbon generation in source rocks, free hydrocarbons undergo short distance primary or secondary migration, occurring in thin interlayers of sandstone. Tight reservoirs can be sandwiched within source rocks or located above and below them, forming a "sandwich" or interbedded structure vertically in Fig. 5(e) and (h). Controlled by organic-rich shale with interlayers of sandstone, quasi-continuous hydrocarbon accumulation mainly developed in the channel front microfacies (LC4 and LC5), and the lower limit of the single-layer thickness of effective tight reservoirs observed in the study area is 0.05 m (Sandstone pores below this lower limit are completely cemented).

(3) Discontinuous hydrocarbon accumulation

According to the traditional oil and gas reservoir formation model, in the case of discontinuous hydrocarbon accumulation, oil and gas generally undergo a migration process to form conventional resources. After the source rock generates hydrocarbons, hydrocarbons undergo secondary migration under the action of formation pressure and oil-water displacement (buoyancy), forming conventional oil with traps as structural units. It is influenced by various factors such as source rock, migration channels, and structural traps. Discontinuous hydrocarbon accumulation mainly developed in the braided channel microfacies (LC6). In the study of hydrocarbon occurrence, evaporation loss of light hydrocarbons is commonly present throughout the entire process of drilling and core sample preservation (Huang et al., 2022; Wei et al., 2024b). Light hydrocarbons rapidly migrate or dissipate due to high sandstone porosity, which may be the reason why the sandstone in LC6 has high porosity but poor oil-bearing properties in the test results of this study.

6. Conclusion

(1) This study first proposes a new depositional model for the mixed sedimentation zone between gravity flow sediments and deep-lacustrine fine-grained sediments in lacustrine rift basins with steep slopes. As the water depth decreases from the center of the basin towards the lake basin edge, there are five microfacies: calcareous semi-deep lake, felsic semi-deep lake, outer fan, channel front and braided channel in the middle fan, influenced by three types of fluids: debris flow, turbidity current, and felsic mixed floating current. There are six types of lithofacies combinations under the control of the five microfacies.

(2) Proposed a sedimentary evolution model for transition zone controlled by astronomical cycles. This study shows the control of 406-kyr long eccentricity cycles on the fluid evolution and sedimentary development of lithofacies combinations in the lake basin. During high eccentricity phases, increased monsoon-driven terrigenous input enhances sandstone deposition, developing braided channel (LC5) and channel front (LC6) microfacies. These intervals exhibit elevated terrigenous quartz/feldspar content and reduced organic carbon in fine-grained sedimentary rocks. Conversely, during low eccentricity phases, felsic mineral layers or isolated sandstone interlayers dominate, forming outer fan (LC3), channel front (LC4), and semi-deep lake (LC1–LC2) microfacies. These intervals show lower terrigenous content and higher TOC in fine-grained sedimentary rocks.

(3) The novel hydrocarbon occurrence model based on the sedimentary evolution model demonstrates the ordered coexistence of conventional and unconventional reservoirs, driven by astronomically forced climate fluctuations. High eccentricity amplifies monsoon-driven sediment influx, forming sandstone-rich lithofacies with discontinuous hydrocarbon accumulation, while low eccentricity stabilizes deposition, favoring organic-rich shales with continuous hydrocarbons accumulation. Based on the differences in hydrocarbon occurrence characteristics of different lithofacies combinations and source-reservoir assemblage types of different sedimentary microfacies controlled by astronomical cycles, the ordered coexistence of shale oil,

tight oil and conventional oil in the study area have been formed. The model offers actionable insights for optimizing exploration in analogous lacustrine rift basins.

CRediT authorship contribution statement

Xian-Xu Fang: Visualization, Formal analysis, Writing – original draft, Investigation, Conceptualization, Writing – review & editing, Methodology, Data curation. **Cun-Fei Ma:** Supervision, Project administration, Funding acquisition, Validation, Resources, Investigation, Software, Methodology. **Feng Qin:** Supervision, Validation, Resources. **Tian-Xia An:** Resources. **Rui-Juan Liu:** Resources. **Hao-Wen Song:** Formal analysis. **Cun-Jian Zhang:** Writing – original draft, Formal analysis. **Tao Wang:** Investigation. **Bo Gao:** Writing – review & editing. **Peng Hao:** Writing – review & editing.

Declaration of competing interest

The authors declare that they have no known competing financial interests or personal relationships that could have appeared to influence the work reported in this paper.

Acknowledgements

This work was funded by Oil & Gas Major Project of China (Grant No. 2024ZD1405102), National Natural Science Foundation of China (Grant No. 42172153), Xinjiang Key Research and Development Program (No. 2024B03007), and Youth Innovation and Technology Support Program for Shandong Provincial Universities (Grant No. 2022KJ066). We would like to thank the Sinopec Shengli Oilfield Company for providing the related core samples and production data in the Paleogene Shahejie Formation, Bohai Bay Basin.

References

Abels, H.A., Aziz, H.A., Calvo, J.P., et al., 2009. Shallow lacustrine carbonate microfacies document orbitally paced lake-level history in the Miocene Teruel basin (North-East Spain). Sedimentology 56, 399–419. https://doi.org/10.1111/j.1365-3091.2008.00976.x.

Abels, H.A., Kraus, M.J., Gingerich, P.D., 2013. Precession-scale cyclicity in the fluvial lower Eocene Willwood formation of the Bighorn Basin, Wyoming (USA). Sedimentology 60, 1467–1483. https://doi.org/10.1111/sed.12039.

Alexandre, J.T., Dirkx, R., Veld, H., et al., 2012. Toarcian black shales in the Dutch central graben: record of energetic, variable depositional conditions during an Oceanic anoxic event. J. Sediment. Res. 82 (2), 104–120. https://doi.org/10.2110/jsr.2012.5.

Aplin, A.C., Macquaker, J.S.H., 2011. Mudstone diversity: Origin and implications for source, seal, and reservoir properties in petroleum systems. AAPG (Am. Assoc. Pet. Geol.) Bull. 95 (12), 2031–2059. https://doi.org/10.1306/03281110162.

Bai, C., Yu, B., Liu, H., et al., 2018. The genesis and evolution of carbonate minerals in shale oil formations from Dongying Depression, Bohai Bay Basin, China. Int. J. Coal Geol. 189, 8–26. https://doi.org/10.1016/j.coal.2018.02.008.

Barrett, E.P., Joyner, L.G., Halenda, P.P., 1951. The determination of pore volume and area distributions in porous substances. I. Computations from nitrogen isotherms. J. Am. Chem. Soc. 73 (1), 373–380. https://doi.org/10.1021/ja01145a126.

Bates, C.C., 1953. Rational theory of delta formation. AAPG (Am. Assoc. Pet. Geol.) Bull. 37 (9), 2119–2162. https://doi.org/10.1306/5CEADD76-16BB-11D7-8645000102C1865D.

Brunauer, S., Emmett, P.H., Teller, E., 1938. Adsorption of gases in multimolecular layers. J. Am. Chem. Soc. 60 (2), 309–319. https://doi.org/10.1021/ja01269a023.

Cantero, M.I., Cantelli, A., Pirmez, C., et al., 2012. Emplacement of massive turbidites linked to extinction of turbulence in turbidity currents. Nat. Geosci. 5, 42–45. https://doi.org/10.1038/ngeo1320.

Cao, Y., Wang, Y., Gluyas, J.G., et al., 2018. Depositional model for lacustrine nearshore subaqueous fans in a rift basin: The Eocene Shahejie Formation, Dongying Sag, Bohai Bay Basin, China. Sedimentology 65, 2117–2148. https://doi.org/10.1111/sed.12459.

Cao, Y., Lin, M., Xi, K., et al., 2024. Bedload transport and deposition of mud-grade sediments in deep-lacustrine settings: A case study in the Triassic Yanchang Formation, Ordos Basin, China. Sedimentology 71, 1984–2008. https://doi.org/10.1111/sed.13200.

Catuneanu, O., 2022. Variability of stratigraphic sequences. In: Catuneanu, O. (Ed.), Principles of Sequence Stratigraphy, second ed. Elsevier, pp. 337–388. https://doi.org/10.1016/B978-0-444-53353-1.00008-0.

Chao, L., Jiang, Z., Cao, Y., et al., 2016. Deep water depositional mechanisms and significance for unconventional hydrocarbon exploration: A case study from the lower Silurian Longmaxi shale in the southeastern Sichuan Basin. AAPG (Am. Assoc. Pet. Geol.) Bull. 5, 773–794. https://doi.org/10.1306/02031615002.

Chen, H., Lin, C., Zhang, Z., et al., 2021. Evolution and controlling factors of the gravity flow deposits in the Miocene sequence stratigraphic framework, the lower Congo Fan Basin, West Africa. Petrol. Explor. Dev. 48 (1), 146–158. https://doi.org/10.1016/S1876-3804(21)60011-3.

Chen, S., Zhang, S., Wang, Y., et al., 2016. Lithofacies types and reservoirs of Paleogene fine-grained sedimentary rocks Dongying Sag, Bohai Bay Basin, China. Petrol. Explor. Dev. 43 (2), 218–229. https://doi.org/10.1016/S1876-3804(16)30025-8.

Chen, Z., Li, M., Cao, T., et al., 2017. Hydrocarbon generation kinetics of a heterogeneous source rock System: Example from the lacsutrine Eocene-Oligocene Shahejie Formation, Bohai Bay Basin, China. Energy Fuel. 31 (12), 13291–13304. https://doi.org/10.1021/acs.energyfuels.7b02361.

Colcord, D.E., Shilling, A.M., Sauer, P.E., et al., 2018. Sub-Milankovitch paleoclimatic and paleoenvironmental variability in East Africa recorded by Pleistocene lacustrine sediments from Olduvai Gorge, Tanzania. Palaeogeogr. Palaeoclimatol. Palaeoecol. 495, 284–291. https://doi.org/10.1016/j.palaeo.2018.01.023.

Dodd, T.J.H., McCarthy, D.J., Richards, P.C., 2019. A depositional model for deep-lacustrine, partially confined, turbidite fans: Early Cretaceous, North Falkland Basin. Sedimentology 66, 53–80. https://doi.org/10.1111/sed.12483.

Dutton, S.P., 2008. Calcite cement in Permian deep-water sandstones, Delaware Basin, west Texas: Origin, distribution, and effect on reservoir properties. AAPG (Am. Assoc. Pet. Geol.) Bull. 92 (6), 765–787. https://doi.org/10.1306/01280807107.

Fang, X., Ma, C., Zhao, L., et al., 2024. Diagenetic evolution of tight sandstone and the formation of an effective reservoir in the lower member 3 of the Shahejie Formation, Bohai Bay Basin, East China. Mar. Petrol. Geol. 161, 106658. https://doi.org/10.1016/j.marpetgeo.2023.106658.

Feng, Y., Zou, C., Li, J., et al., 2021. Sediment gravity-flow deposits in Late Cretaceous Songliao postrift downwarped lacustrine Basin, Northeastern China. Mar. Petrol. Geol. 134, 105378. https://doi.org/10.1016/j.marpetgeo.2021.105378.

Garcia-Hidalgo, J.F., Gil, J., Segura, M., et al., 2007. Internal anatomy of a mixed siliciclastic-carbonate platform: the late Cenomanian-Mid Turonian at the southern margin of the Spanish central system. Sedimentology 54, 1245–1271. https://doi.org/10.1111/j.1365-3091.2007.00880.x.

Gorynski, K.E., Tobey, M.H., Enriquez, D.A., et al., 2019. Quantification and characterization of hydrocarbon-filled porosity in oil-rich shales using integrated thermal extraction, pyrolysis, and solvent extraction. AAPG (Am. Assoc. Pet. Geol.) Bull. 103 (3), 723–744. https://doi.org/10.1306/08161817214.

Gregg, S.J., Sing, K.S.W., 1982. Adsorption, surface area and porosity. In: Haul, R. (Ed.), Berichte Der Bunsengesellschaft Für Physikalische Chemie, second ed. Auflage, Academic Press, London, p. 957. https://doi.org/10.1002/bbpc.19820861019. 957.

Guo, X., Liu, K., He, S., et al., 2012. Petroleum generation and charge history of the northern Dongying depression, Bohai Bay Basin, China: insight from integrated fluid inclusion analysis and basin modelling. Mar. Petrol. Geol. 32 (1), 21–35. https://doi.org/10.1016/j.marpetgeo.2011.12.007.

Guo, X., Ma, X., Li, M., et al., 2023. Mechanisms for lacustrine shale oil enrichment in Chinese sedimentary basins. Oil Gas Geol. 44, 1333–1349. https://doi.org/10.11743/ogg20230601 (in Chinese).

Hickey, J.J., Henk, B., 2007. Lithofacies summary of the Mississippian Barnett Shale, mitchell 2 TP sims well, Wise County, Texas. AAPG (Am. Assoc. Pet. Geol.) Bull. 91 (4), 437–443. https://doi.org/10.1306/12040606053.

Hou, L., Pang, Z., Luo, X., et al., 2023. Sedimentary features of the gravity flow influenced shale deposit: A case study of Chang 7 member in the Ordos Basin, China. Mar. Petrol. Geol. 153, 106277. https://doi.org/10.1016/j.marpetgeo.2023.106277.

Hu, Q., Zhang, Y., Meng, X., et al., 2017. Characterization of multiple micro-nano pore networks in shale oil reservoirs of Paleogene Shahejie Formation in Dongying Sag of Bohai Bay Basin, East China. Petrol. Explor. Dev. 44 (5), 720–730. https://doi.org/10.1016/S1876-3804(17)30083-6.

Hu, Q., Wang, Q., Zhang, T., et al., 2023. Petrophysical properties of representative geological rocks encountered in carbon storage and utilization. Energy Rep. 9, 3661–3682. https://doi.org/10.1016/j.egyr.2023.02.020.

Hu, T., Jiang, F., Pang, X., et al., 2024. Identification and evaluation of shale oil micro-migration and its petroleum geological significance. Petrol. Explor. Dev. 51 (1), 127–140. https://doi.org/10.1016/S1876-3804(24)60010-8.

Huang, C., Hinnov, L., Fischer, A.G., et al., 2010. Astronomical tuning of the Aptian Stage from Italian reference sections. Geology 38 (10), 899–902. https://doi.org/10.1130/G31177.1.

Huang, C., Hinnov, L., 2019. Astronomically forced climate evolution in a saline lake record of the middle Eocene to Oligocene, Jianghan Basin, China. Earth Planet Sci. Lett. 528, 115846. https://doi.org/10.1016/j.epsl.2019.115846.

Huang, Y., Liao, Y., Pan, Y., et al., 2022. Improved light hydrocarbons collection method for the pyrolysis of crude oil in gold tube closed system experiments. Org. Geochem. 168, 104432. https://doi.org/10.1016/j.orggeochem.2022.104432.
Jarvie, D.M., 1991. Total Organic Carbon (TOC) analysis. In: Merrill, R.K. (Ed.), Source and Migration Processes and Evaluation Techniques. American Association of Petroleum Geologists. https://doi.org/10.1306/TrHbk543C11.
Jiang, Q., Li, M., Qian, M., et al., 2016. Quantitative characterization of shale oil in different occurrence states and its application. Petrol. Geol. Exp. 38 (6), 842–849. https://doi.org/10.11781/sysydz201606842 (in Chinese).
Jiang, Z., Liang, S., Zhang, Y., et al., 2014. Sedimentary hydrodynamic study of sand bodies in the upper subsection of the 4th Member of the Paleogene Shahejie Formation in the eastern Dongying Depression, China. Pet. Sci. 11, 189–199. https://doi.org/10.1007/s12182-014-0332-7.
Jiang, Z., Duan, H., Liang, C., et al., 2017. Classification of hydrocarbon-bearing fine-grained sedimentary rocks. J. Earth Sci. 28, 693–976. https://doi.org/10.1007/s12583-016-0920-0.
Jin, S., Liu, S., Li, Z., et al., 2022. Astrochronology of a middle Eocene lacustrine sequence and sedimentary noise modeling of lake-level changes in Dongying depression, Bohai Bay Basin. Palaeogeogr. Palaeoclimatol. Palaeoecol. 585, 110740. https://doi.org/10.1016/j.palaeo.2021.110740.
Joerg, R., Martin, K., 2020. Soil particle density as affected by soil texture and soil organic matter: 2. Predicting the effect of the mineral composition of particle-size fractions. Geoderma 375, 114543. https://doi.org/10.1016/j.geoderma.2020.114543.
Katz, A.J., Thompson, A.H., 1987. Prediction of rock electrical conductivity from mercury injection measurements. J. Geophys. Res. Solid Earth 92 (B1), 599–607. https://doi.org/10.1029/JB092iB01p00599.
Kouassi, L.K., Qiu, L., Yang, Y., et al., 2022. Depositional and diagenetic control on conglomerate reservoirs: an example from the fourth member of shahejie formation in the Lijin Sag, Bohai Bay Basin, East China. J. Petrol. Sci. Eng. 218, 110913. https://doi.org/10.1016/j.petrol.2022.110913.
Kuila, U., Prasad, M., 2013. Specific surface area and pore-size distribution in clays and shales. Geophys. Prospect. 61, 341–362. https://doi.org/10.1111/1365-2478.12028.
Laskar, J., Robutel, P., Joutel, F., et al., 2004. A long-term numerical solution for the insolation quantities of the Earth. Astron. Astrophys. 428 (1), 261–285. https://doi.org/10.1051/0004-6361:20041335.
Laskar, J., Fienga, A., Gastineau, M., et al., 2011. La2010: a new orbital solution for the long-term motion of the Earth. Astron. Astrophys. 532, 15. https://doi.org/10.1051/0004-6361/201116836.
Law, B.E., 2002. Basin-centered gas systems. AAPG (Am. Assoc. Pet. Geol.) Bull. 86, 1891–1919. https://doi.org/10.1306/61EEDDB4-173E-11D7-8645000102C1865D.
Law, B.E., Curtis, J.B., 2002. Introduction to unconventional petroleum systems. AAPG (Am. Assoc. Pet. Geol.) Bull. 86 (11), 1851–1852. https://doi.org/10.1306/61EEDDA0-173E-11D7-8645000102C1865D.
Li, B., Pang, X., Dong, Y., et al., 2019. Lithofacies and pore characterization in an argillaceous-siliceous-calcareous shale system: A case study of the Shahejie Formation in Nanpu Sag, Bohai Bay Basin, China. J. Petrol. Sci. Eng. 173. https://doi.org/10.1016/j.petrol.2018.10.086.
Li, J., Zhen, M., Chen, X., et al., 2015. Connotation analysis, source-reservoir assemblage types and development potential of unconventional hydrocarbons in China. Petrol. Res. 1 (2), 135–148. https://doi.org/10.1016/S2096-2495(17)30038-8.
Li, J., Jiang, C., Wang, M., et al., 2020. Adsorbed and free hydrocarbons in unconventional shale reservoir: A new insight from NMR T1-T2 maps. Mar. Petrol. Geol. 116, 104311. https://doi.org/10.1016/j.marpetgeo.2020.104311.
Li, M., Kump, L.R., Hinnov, L.A., et al., 2018. Tracking variable sedimentation rates and astronomical forcing in Phanerozoic paleoclimate proxy series with evolutionary correlation coefficients and hypothesis testing. Earth Planet Sci. Lett. 501, 165–179. https://doi.org/10.1016/j.epsl.2018.08.041.
Li, M., Hinnov, L., Kump, L., 2019. Acycle: Time-series analysis software for paleoclimate research and education. Comput. Geosci. 127, 12–22. https://doi.org/10.1016/j.cageo.2019.02.011.
Liang, C., Cao, Y., Jiang, Z., et al., 2017. Shale oil potential of lacustrine Black shale in the Eocene dongying depression: Implications for geochemistry and Reservoir characteristics. AAPG (Am. Assoc. Pet. Geol.) Bull. 101 (11), 1835–1858. https://doi.org/10.1306/01251715249.
Liang, C., Wu, J., Cao, Y., et al., 2022. Storage space development and hydrocarbon occurrence model controlled by lithofacies in the Eocene Jiyang Sub-basin, East China: Significance for shale oil reservoir formation. J. Petrol. Sci. Eng. 215, 110631. https://doi.org/10.1016/j.petrol.2022.110631.
Liang, C., Yang, B., Cao, Y., et al., 2024. Salinisation mechanism of lakes and controls on organic matter enrichment: from present to deep-time. Earth Sci. Rev. 251, 104720. https://doi.org/10.1016/j.earscirev.2024.104720.
Licht, A., Cappelle, M., Abels, H.A., et al., 2014. Asian monsoons in a late Eocene greenhouse world. Nature 513, 501–506. https://doi.org/10.1038/nature13704.
Lin, J., Dong, C., Lin, C., et al., 2024. The impact of tectonic inversion on diagenesis and reservoir quality of the Oligocene fluvial sandstones: The Upper Huagang Formation, Xihu Depression, East China Sea Shelf Basin. Mar. Petrol. Geol. 165, 106860. https://doi.org/10.1016/j.marpetgeo.2024.106860.
Lineback, J.A., 1968. Subdivisions and depositional environments of new albany shale (Devonian-Mississippian) in Indiana. AAPG (Am. Assoc. Pet. Geol.) Bull. 52 (7), 1291–1303. https://doi.org/10.1306/5D25C4AB-16C1-11D7-8645000102C1865D.
Liu, B., Wang, H., Fu, X., et al., 2019. Lithofacies and depositional setting of a highly prospective lacustrine shale oil succession from the Upper Cretaceous Qingshankou Formation in the Gulong sag, northern Songliao Basin, northeast China. AAPG (Am. Assoc. Pet. Geol.) Bull. 103 (2), 405–432. https://doi.org/10.1306/08031817416.
Liu, K., Ostadhassan, M., 2019. The impact of pore size distribution data presentation format on pore structure interpretation of shales. Adv. Geo-Energy Res. 3 (2), 187–197. https://doi.org/10.26804/ager.2019.02.08.
Liu, Z., Huang, C., Algeo, T.J., et al., 2018. High-resolution astrochronological record for the Paleocene-Oligocene (66–23Ma) from the rapidly subsiding Bohai Bay Basin, Northeastern China. Palaeogeogr. Palaeoclimatol. Palaeoecol. 510, 78–92. https://doi.org/10.1016/j.palaeo.2017.10.030.
Loucks, R.G., Ruppel, S.C., 2007. Mississippian Barnett Shale: Lithofacies and depositional setting of a deep-water shale-gas succession in the Fort Worth Basin, Texas. AAPG (Am. Assoc. Pet. Geol.) Bull. 91 (4), 579–601. https://doi.org/10.1306/11020606059.
Loucks, R.G., Reed, R.M., Ruppel, S.C., et al., 2012. Spectrum of pore types and networks in mudrocks and a descriptive classification for matrix-related mudrock pores. AAPG (Am. Assoc. Pet. Geol.) Bull. 96 (6), 1071–1098. https://doi.org/10.1306/08171111061.
Lu, Y., Sun, Y., Weng, H., 2004. Lacustrine sediments as a record of changes of regional climate and environment. Geochimica 33 (1), 20–26. https://doi.org/10.3321/j.issn:0379-1726.2004.01.003 (in Chinese).
Ma, B., Cao, Y., Eriksson, K.A., et al., 2017. Depositional and diagenetic controls on deeply-buried Eocene sublacustrine fan reservoirs in the dongying depression, Bohai Bay Basin, China. Mar. Petrol. Geol. 82, 297–317. https://doi.org/10.1016/j.marpetgeo.2017.02.014.
Ma, C., Huang, W., Du, Z., et al., 2022. Shale lithofacies classification scheme of continental lake basin and its significance: a case of E_2 Member of Kongdian Formation in Cangdong Sag. J. Centr. South Univ. Sci. Technol. 53 (9), 3287–3300. https://doi.org/10.11817/j.issn.1672-7207.2022.09.002 (in Chinese).
Ma, Y., Fan, M., Li, M., et al., 2023. East Asian lake hydrology modulated by global sea-level variations in the Eocene warmhouse. Earth Planet Sci. Lett. 602, 117925. https://doi.org/10.1016/j.epsl.2022.117925.
Ma, C., Fang, X., Ma, X., et al., 2023. Properties and model of a lacustrine shale oil reservoir: a case Study of the upper fourth member and lower third member of the Shahejie Formation in dongying Sag and Zhanhua Sag, Jiyang Depression. J. Mar. Sci. Eng. 11 (7), 1441. https://doi.org/10.3390/jmse11071441.
Ma, C., Fang, X., Wu, Y., et al., 2024. Target-based sedimentary diagenesis simulation and three-dimensional diagenesis evolution modeling. Mar. Petrol. Geol. 160, 106597. https://doi.org/10.1016/j.marpetgeo.2023.106597.
Machlus, M.L., Olsen, P.E., Christie-Blick, N., et al., 2008. Spectral analysis of the lower eocene wilkins peak member, green river formation, Wyoming: Support for Milankovitch cyclicity. Earth Planet Sci. Lett. 268, 64–75. https://doi.org/10.1016/j.epsl.2007.12.024.
Masters, J.A., 1979. Deep basin gas trap, Western Canada. AAPG (Am. Assoc. Pet. Geol.) Bull. 63 (2), 152–181. https://doi.org/10.1306/C1EA55CB-16C9-11D7-8645000102C1865D.
Mount, J.F., 1984. Mixing of siliciclastic and carbonate sediments in shallow shelf environments. Geology 12 (7), 432–435. https://doi.org/10.1130/0091-7613(1984)12<432:MOSACS>2.0.CO;2.
Mulder, T., Syvitski, J.P.M., Migeon, S., et al., 2003. Marine hyperpycnal flows: initiation, behavior and related deposits. Mar. Petrol. Geol. 20, 861–882. https://doi.org/10.1016/j.marpetgeo.2003.01.003.
Niu, X., Yang, T., Cao, Y., et al., 2023. Characteristics and formation mechanisms of gravity-flow deposits in a lacustrine depression basin: Examples from the Late Triassic Chang 7 oil member of the Yanchang Formation, Ordos Basin, Central China. Mar. Petrol. Geol. 148, 106048. https://doi.org/10.1016/j.marpetgeo.2022.106048.
Ougier-Simonin, A., Renard, F., Boehm, C., et al., 2016. Microfracturing and microporosity in shales. Earth Sci. Rev. 162, 198–226. https://doi.org/10.1016/j.earscirev.2016.09.006.
Palermo, D., Aigner, T., Geluk, M., et al., 2008. Reservoir potential of a lacustrine mixed carbonate/siliciclastic gas reservoir: the Lower Triassic Rogenstein in the Netherlands. J. Petrol. Geol. 31, 61–95. https://doi.org/10.1111/j.1747-5457.2008.00407.x.
Pälike, H., Shackleton, N.J., Röhl, U., 2001. Astronomical forcing in late Eocene marine sediments. Earth Planet Sci. Lett. 193, 589–602. https://doi.org/10.1016/S0012-821X(01)00501-5.
Pan, S., Guo, Q., Zou, C., et al., 2023. Identification of sweet spots in shale-type and siltstone-type “shale oil systems”: A case study of the Chang 7 member in Ordos Basin. Sci. China Earth Sci. 66, 1647–1663. https://doi.org/10.1007/s11430-022-1042-x.
Pang, X., Shao, X., Li, M., et al., 2021. Correlation and difference between conventional and unconventional reservoirs and their unified genetic classification. Gondwana Res. 97, 73–100. https://doi.org/10.1016/j.gr.2021.04.011.
Ping, H., Chen, H., Jia, G., 2017. Petroleum accumulation in the deeply buried reservoirs in the northern Dongying Depression, Bohai Bay Basin, China: New insights from fluid inclusions, natural gas geochemistry, and 1-D basin modeling. Mar. Petrol. Geol. 80, 70–93. https://doi.org/10.1016/j.marpetgeo.2016.11.023.
Plantz, J.B., Sedorko, D., Carelli, T.G., et al., 2024. Depositional processes in a shale-dominated Devonian succession: Sedimentary facies and trace fossil

integrated analysis. Sediment. Geol. 470, 106716. https://doi.org/10.1016/j.sedgeo.2024.106716.
Pranter, M.J., Sommer, N.K., 2011. Static connectivity of fluvial sandstones in a lower coastal-plain setting: an example from the Upper Cretaceous lower Williams Fork Formation, Piceance Basin, Colorado. AAPG (Am. Assoc. Pet. Geol.) Bull. 95 (6), 899–923. https://doi.org/10.1306/12091010008.
Robinson, D.A., Thomas, A., Reinsch, S., et al., 2022. Analytical modelling of soil porosity and bulk density across the soil organic matter and land-use continuum. Sci. Rep. 12, 7085. https://doi.org/10.1038/s41598-022-11099-7.
Selley, R.C., Sonnenberg, S.A., 2015. Sedimentary basins and petroleum systems. In: Selley, R.C., Sonnenberg, S.A. (Eds.), Elements of Petroleum Geology, third ed. Academic Press, Waltham, pp. 377–426. https://doi.org/10.1016/B978-0-12-386031-6.00008-4.
Shanmugam, G., 2018. A global satellite survey of density plumes at river mouths and at other environments: plume configurations, external controls, and implications for deep-water sedimentation. Petrol. Explor. Dev. 45 (4), 640–661. https://doi.org/10.1016/S1876-3804(18)30069-7.
Shen, C., Ren, L., Zhao, J., et al., 2021. Division of shale lithofacies associations and their impact on fracture network formation in the Silurian Longmaxi Formation, Sichuan Basin. Oil Gas Geol. 42 (1), 98–106+123. https://doi.org/10.11743/ogg20210109 (in Chinese).
Shi, J., Jin, J., Liu, Q., et al., 2019. Cyclostratigraphy and astronomical tuning of the middle eocene terrestrial successions in the Bohai Bay Basin, Eastern China. Global Planet. Change 174, 115–126. https://doi.org/10.1016/j.gloplacha.2019.01.001.
Shi, J., Jin, Z., Liu, Q., et al., 2020. Depositional process and astronomical forcing model of lacustrine fine-grained sedimentary rocks: A case study of the early Paleogene in the Dongying Sag, Bohai Bay Basin. Mar. Petrol. Geol. 113, 103995. https://doi.org/10.1016/j.marpetgeo.2019.08.023.
Shu, Y., Bao, H., Zheng, Y., et al., 2021. Lithofacies types, assemblage characteristics, and sedimentary evolution model of lacustrine shale in Dongyuemiao Formation of fuxing area. Front. Earth Sci. 9. https://doi.org/10.3389/feart.2021.772581.
Sing, K.S.W., 1985. Reporting physisorption data for gas/solid systems with special reference to the determination of surface area and porosity (recommendations 1984). Pure Appl. Chem. 57 (4), 603–619. https://doi.org/10.1351/pac198557040603.
Slatt, R.M., O'Brien, N.R., 2011. Pore types in the Barnett and Woodford gas shales: contribution to understanding gas storage and migration pathways in fine-grained rocks. AAPG (Am. Assoc. Pet. Geol.) Bull. 95 (12), 2017–2030. https://doi.org/10.1306/03301110145.
Smith, L.B., Schieber, J., Wilson, R.D., 2019. Shallow-water onlap model for the deposition of Devonian black shales in New York, USA. Geology 47 (3), 279–283. https://doi.org/10.1130/G45569.1.
Smith, M.E., Carroll, A.R., Scott, J.J., et al., 2014. Early Eocene carbon isotope excursions and landscape destabilization at eccentricity minima: Green River Formation of Wyoming. Earth Planet Sci. Lett. 403, 393–406. https://doi.org/10.1016/j.epsl.2014.06.024.
Song, X., Zhou, X., Lv, X., 2023. Quantitative evaluation of pore connectivity of shales with a type H3 sorption hysteresis loop. J. Asian Earth Sci. 247, 105595. https://doi.org/10.1016/j.jseaes.2023.105595.
Sun, S., Liu, H., Cao, Y., et al., 2017. Milankovitch cycle of lacustrine deepwater fine-grained sedimentary rocks and its significance to shale oil: a case study of the upper Es4 member of well NY1 in Dongying Sag. J. China Univ. Min. Technol. 46 (4), 846–858. https://doi.org/10.13247/j.cnki.jcumt.000638 (in Chinese).
Sun, Z., Jiang, T., Zhu, H., et al., 2023. Reconstruction of lake-level changes by sedimentary noise modeling (Dongying depression, late Eocene, East China). Energies 16 (5), 2216. https://doi.org/10.3390/en16052216.
Thomson, D.J., 1982. Spectrum estimation and harmonic analysis. Proc. IEEE 70 (9), 1055–1096. https://doi.org/10.1109/PROC.1982.12433.
Walker, R.G., 1978. Deep-water sandstone facies and ancient submarine fans: models for exploration for stratigraphic traps. AAPG (Am. Assoc. Pet. Geol.) Bull. 62 (6), 932–966. https://doi.org/10.1306/C1EA4F77-16C9-11D7-8645000102C1865D.
Wang, D., Wu, S., Wang, Y., et al., 2015. Deep-water sediment cycles in the Qiongdongnan basin. Chin. Sci. Bull. 60 (10), 933–943. https://doi.org/10.1360/N972014-00477.
Wang, J., Jiang, Z., Zhang, Y., et al., 2016a. Quantitative evaluation of the reservoir potential and controlling factors of semi-deep lacustrine tempestites in the Eocene Lijin Sag of the Bohai Bay Basin, East China. Mar. Petrol. Geol. 77, 262–279. https://doi.org/10.1016/j.marpetgeo.2016.05.006.
Wang, M., Chen, H., Huang, Chunju, et al., 2020b. Astronomical forcing and sedimentary noise modeling of lake-level changes in the Paleogene Dongpu Depression of North China. Earth Planet Sci. Lett. 535, 116116. https://doi.org/10.1016/j.epsl.2020.116116.
Wang, S., Javadpour, F., Feng, Q.H., 2016c. Confinement correction to mercury intrusion capillary pressure of shale nanopores. Sci. Rep. 6, 20160. https://doi.org/10.1038/srep20160.
Wang, W., Yue, D., Eriksson, K.A., et al., 2020a. Qualitative and quantitative characterization of multiple factors that influence movable fluid saturation in lacustrine deep-water gravity-flow tight sandstones from the Yanchang Formation, southern Ordos Basin, China. Mar. Petrol. Geol. 121, 104625. https://doi.org/10.1016/j.marpetgeo.2020.104625.
Wang, Y., Cao, Y., Ma, B., et al., 2014. Mechanism of diagenetic trap formation in nearshaore subaqueous fans on steep rift lacustrine basin slopes. Pet. Sci. 11, 481–494. https://doi.org/10.1007/s12182-014-0364-z.
Wang, Y., Cao, Y., Zhang, S., et al., 2016b. Genetic mechanisms of secondary pore development zones of Es4xin the north zone of the Minfeng Sag in the Dongying Depression, East China. Pet. Sci. 13, 1–17. https://doi.org/10.1007/s12182-016-0076-7.
Washburn, E.W., 1921. Note on a method of determining the distribution of pore sizes in a porous material. Proc. Natl. Acad. Sci. U. S. A. 7 (4), 115–116. https://doi.org/10.1073/pnas.7.4.115.
Wei, W., Kemp, D.B., Lu, Y., et al., 2024a. Astronomically forcing salinity variations in a marginal-marine environment, Bohai Bay Basin, NE China. Chem. Geol. 665, 122300. https://doi.org/10.1016/j.chemgeo.2024.122300.
Wei, Z., He, Z., Yang, J., 2024b. Analysis of core temperature variation and its influencing factors in deep rock in-situ temperature-preserved coring. Adv. Geo-Energy Res. 14 (3), 215–223. https://doi.org/10.46690/ager.2024.12.06.
Westerhold, T., Röhl, U., Laskar, J., 2012. Time scale controversy: Accurate orbital calibration of the early Paleogene. G-cubed 13. https://doi.org/10.1029/2012GC004096.
Westerhold, T., Marwan, N., Drury, A.J., et al., 2020. An astronomically dated record of Earth's climate and its predictability over the last 66 million years. Science 369, 1383–1387. https://doi.org/10.1126/science.aba6853.
Wu, H., Zhang, S., Hinnov, L.A., et al., 2014. Cyclostratigraphy and orbital tuning of the terrestrial upper Santonian-Lower Danian in Songliao Basin, Northeastern China. Earth Planet Sci. Lett. 407, 82–95. https://doi.org/10.1016/j.epsl.2014.09.038.
Xi, K., Cao, Y., Zhu, R., et al., 2015. Rock types and characteristics of tight oil reservoir in Permian Lucaogou Formation, Jimsar sag. Acta Petrol. Sin. 36, 1495–1507. https://doi.org/10.7623/syxb201512004 (in Chinese).
Xian, B., Wang, Y., Zhou, T., et al., 2007. Distribution and controlling factors of glutinite bodies in the actic region of a rift basin: An example from Chezhen Sag, Bohai Bay Basin. Petrol. Explor. Dev. 34, 429–436. https://doi.org/10.1016/S1872-5813(07)60034-6 (in Chinese).
Xu, T., Peng, J., Yu, L., et al., 2023. The control of astronomical cycles on lacustrine fine-grained event Sedimentation—A case study of the Chunshang submember of the upper Es4 in the Dongying Sag. Pet. Sci. 20, 1395–1410. https://doi.org/10.1016/j.petsci.2022.11.023.
Yang, S., Qiao, H., Cheng, B., et al., 2021. Solvent extraction efficiency of an Eocene-aged organic-rich lacustrine shale. Mar. Petrol. Geol. 126, 104941. https://doi.org/10.1016/j.marpetgeo.2021.104941.
Yang, T., Cao, Y., Friis, H., et al., 2018. Genesis and distribution pattern of carbonate cements in lacustrine deep-water gravity-flow sandstone reservoirs in the third member of the Shahejie Formation in the Dongying Sag, Jiyang depression, Eastern China. Mar. Petrol. Geol. 92, 547–564. https://doi.org/10.1016/j.marpetgeo.2017.11.020.
Yerejiepu, H., Wang, X., Qiu, L., et al., 2024. Lithofacies characteristics and genetic mechanism of hybrid sedimentary rocks in Da'anzhai member, Sichuan Basin. Mar. Petrol. Geol. 162, 106695. https://doi.org/10.1016/j.marpetgeo.2024.106695.
Yuan, B., Song, W., Chen, Y., et al., 2025. Numerical simulation of fracture flow regulation by gel particles and optimization methods for injection parameters in low-permeability reservoirs. J. China Univ. Petrol. (Ed. Nat. Sci.) 49 (3), 10–18. https://doi.org/10.3969/j.issn.1673-5005.2025.03.002 (in Chinese).
Zagorski, W.A., 1988. Exploration concepts and methodology for deep Medina sandstone reservoirs in northwestern Pennsylvania. AAPG (Am. Assoc. Pet. Geol.) Bull. 72, 976.
Zhang, C., Hu, Q., Yang, S., et al., 2024a. Hierarchical cluster and principal component analyses of multi-scale pore structure and shale components in the Upper Triassic Chang 7 Member in the Ordos Basin of Northern China. J. Asian Earth Sci. 261, 106001. https://doi.org/10.1016/j.jseaes.2023.106001.
Zhang, J., Jiang, Z., Jiang, X., et al., 2016. Oil generation induces sparry calcite formation in lacustrine mudrock, Eocene of east China. Mar. Petrol. Geol. 71, 344–359. https://doi.org/10.1016/j.marpetgeo.2016.01.007.
Zhang, J., Zhong, Q., Wang, F., et al., 2024b. Application of astronomical cycle theory to sedimentary evolution and sweet spot prediction of shale oil-gas reservoir. Acta Pet. Sin. 45 (10), 1507–1521. https://doi.org/10.7623/syxb202410005, 1551 (in Chinese).
Zhang, S., Cao, Y., Zhu, R., et al., 2018. Lithofacies classification of fine-grained mixed sedimentary rocks in the permian lucaogou formation, jimsar sag, junggar basin. Earth Sci. Front. 25, 198–209. https://doi.org/10.13745/j.esf.yx.2017-5-2 (in Chinese).
Zhao, J., Cao, Q., Bai, Y., et al., 2017. Petroleum accumulation: from the continuous to discontinuous. Petrol. Res. 2 (2), 131–145. https://doi.org/10.1016/j.ptlrs.2017.02.001.
Zhao, L., Liu, B., Wen, Z., et al., 2025. Astronomical forcing of lake-level changes along the low-latitude Asian continental margin and the global sea level responses during the early-middle Eocene. J. Asian Earth Sci. 280, 106470. https://doi.org/10.1016/j.jseaes.2024.106470.
Zhao, T., Xu, S., Hao, F., 2023. Differential adsorption of clay minerals: implications for organic matter enrichment. Earth Sci. Rev. 246, 104598. https://doi.org/10.1016/j.earscirev.2023.104598.
Zou, C., 2017. Shale oil and gas. In: Zou, C. (Ed.), Unconventional Petroleum Geology, second ed. Elsevier, pp. 275–321. https://doi.org/10.1016/B978-0-12-812234-1.00010-8.
Zou, C., Yang, Z., Zhang, G., et al., 2014. Conventional and unconventional petroleum "orderly accumulation": Concept and practical significance. Petrol. Explor. Dev. 41 (1), 14–30. https://doi.org/10.1016/S1876-3804(14)60002-1.